TITLE PAGE

Heterozygosity for neurodevelopmental disorder-associated *TRIO* variants yields distinct deficits in behavior, neuronal development, and synaptic transmission in mice

Yevheniia Ishchenko*[1], Amanda T. Jeng*[1,2], Shufang Feng[1,3], Timothy Nottoli[4], Cindy Manriquez-Rodriguez[5], Khanh Nguyen[5], Melissa G. Carrizales[1], Matthew J. Vitarelli[1], Ellen E. Corcoran[1], Charles A. Greer[6,7], Samuel A. Myers[5], Anthony J. Koleske[1,2,6]

1. Department of Molecular Biophysics and Biochemistry, Yale University, New Haven, CT, USA
2. Interdepartmental Neuroscience Program, Yale University, New Haven, CT, USA
3. Department of Medical Psychology, The Third Medical Center, Chinese PLA General Hospital, Beijing, China
4. Department of Comparative Medicine, Yale School of Medicine, New Haven, CT, USA
5. Laboratory for Immunochemical Circuits, La Jolla Institute for Immunology, La Jolla, CA, USA
6. Department of Neuroscience, Yale School of Medicine, New Haven, CT, USA
7. Department of Neurosurgery, Yale School of Medicine, New Haven, CT, USA

* These authors contributed equally to this work.

ABSTRACT

Heterozygosity for rare genetic variants in *TRIO* is associated with neurodevelopmental disorders (NDDs) including schizophrenia (SCZ), autism spectrum disorder (ASD) and intellectual disability. TRIO uses its two guanine nucleotide exchange factor (GEF) domains to activate GTPases (GEF1: Rac1 and RhoG; GEF2: RhoA) that control neuronal migration, synapse development and function. It remains unclear whether and how discrete *TRIO* variants differentially impact these neurodevelopmental events. Here, we elucidate how heterozygosity for NDD-associated *Trio* variants – *+/K1431M* (ASD), *+/K1918X* (SCZ), and *+/M2145T* (bipolar disorder, BPD) – impact mouse behavior, brain development, and synapse structure and function. Heterozygosity for different *Trio* variants impacts motor, social, and cognitive behaviors in distinct ways that align with clinical phenotypes in humans. ASD- and SCZ-linked *Trio* variants differentially impact head and brain size with corresponding changes in dendritic arbors of motor cortex layer 5 pyramidal neurons (M1 L5 PNs). Although dendritic spine density and synaptic ultrastructure were only modestly altered in the *Trio* variant heterozygotes, we observe significant changes in synaptic function and plasticity including excitatory/inhibitory imbalance and long-term potentiation defects. We also identify distinct changes in glutamate synaptic release in *+/K1431M* and *+/M2145T* cortico-cortical synapses, associated with deficiencies in crucial presynaptic release regulators. While *TRIO K1431M* has impaired ability to promote GTP exchange on Rac1, *+/K1431M* mice exhibit increased Rac1 activity, suggesting possible compensation by other GEFs. Our work reveals that discrete disease-associated *Trio* variants yield overlapping but distinct NDD-associated phenotypes in mice and demonstrates, for the first time, an essential role for Trio in presynaptic glutamate release, underscoring the importance of studying the impact of variant heterozygosity in vivo.

INTRODUCTION

Neurodevelopmental disorders (NDDs), including autism spectrum disorder (ASD), intellectual disability (ID), developmental delay (DD), schizophrenia (SCZ) and bipolar disorder (BPD), disrupt brain development and function. While these are diagnostically distinct disorders (1), NDDs share considerable comorbidities and present with overlapping symptoms, including impairments in cognition, behavior, language, social and motor skills, emotions, and learning ability. In addition, the risk genes for NDDs overlap significantly, further suggesting overlap in the mechanistic underpinnings and pathology of these disorders (2-7). The major challenge remains in understanding how diverse risk-conferring variants contribute to the pathophysiology of various NDDs.

TRIO is highly expressed in the developing mammalian brain (8-12), where it is crucial in neuronal migration and morphogenesis, axon guidance, dendritic arbor and spine formation, synaptogenesis, postsynaptic function, and ultimately neuronal circuits impacting cognitive function (13-21). Mice with complete or neuronal-specific knockout of *Trio* exhibit decreased survival and abnormal skeletal muscle and neural tissue disorganization in several brain regions (22-24). Trio is critical for proper development and function of both excitatory and inhibitory neurons, as selective ablation of *Trio* in either neuron type alters morphology, impairs synaptic signaling, and yields NDD-related behavioral defects (25, 26). Trio regulates synaptic strength at excitatory synapses through AMPA receptor trafficking, and its deficiency leads to aberrations in long-term potentiation (LTP), important for learning and memory (25, 27, 28).

Damaging *de novo* mutations and ultra-rare variants in *TRIO* are enriched in individuals with NDDs (8, 9, 29-34). *TRIO* encodes a large cytoskeletal regulatory protein with two guanine nucleotide exchange factor (GEF) domains for Rho family GTPases - GEF1 activates Rac1 and RhoG, while GEF2 activates RhoA (35-37). As a dual RhoGEF, TRIO integrates signals downstream of cell surface receptors and acts on GTPases to coordinate cytoskeletal rearrangements critical for proper neurodevelopment (16, 28, 38-44). Interestingly, nonsense variants spread throughout *TRIO* are enriched in individuals with SCZ (34, 45), whereas pathogenic missense *TRIO* variants in or surrounding the GEF1 domain are associated with ASD/ID (9, 32, 33). Of these, variants in GEF1 that decrease Rac1 activation are associated with milder ID and microcephaly, whereas variants in the adjacent spectrin repeat 8 domain that increase Rac1 activation are associated with a more severe ID and macrocephaly (29, 30, 46, 47). Rare missense variants in *TRIO* have also been observed in BPD, epilepsy, and other disorders, but studies to date are underpowered to establish a causal link with these disorders.

Given the wide spectrum of *TRIO* variants associated with different pathological conditions, a fundamental and unresolved question is how distinct *TRIO* variants differentially impact

mammalian brain development. NDD-associated *TRIO* variants affect GEF1 and GEF2 activities, cell morphology, inhibitory neuron maturation, axon guidance, and synapse function (25-27, 29, 30, 47); however, the impact of heterozygosity for distinct *TRIO* variants in vivo, as found in individuals with NDDs, has been largely unexplored.

We report here the comprehensive analysis of mice heterozygous for discrete *Trio* variants associated with different NDDs: ASD-associated *+/K1431M* in the Trio GEF1 domain, SCZ-associated *+/K1918X*, and BPD-associated *+/M2145T* in Trio GEF2 domain. We show that distinct *Trio* NDD-associated variants differentially impair mouse behavior, brain development, and inhibitory and excitatory synaptic transmission. We show, for the first time, that *Trio* variants that impact GEF1 and GEF2 activity differentially impact presynaptic neurotransmitter release and synaptic vesicle replenishment. Together, our data show how discrete heterozygous *TRIO* variants that impact either Trio protein levels or GEF1/GEF2 catalytic activity yield divergent effects on behavior, neurodevelopment, and synaptic transmission.

MATERIALS AND METHODS

Animal work

All animal-related work was performed in compliance with federal guidelines and approved by the Yale University Institutional Animal Care and Use Committee. Age-matched male and female mice were used for all behavioral experiments. We used only male mice for electrophysiological and neuroanatomical studies to reduce potential variation due to estrus cycle (48).

Generation of *Trio* mutant mice

Trio variant mice were generated via CRISPR/Cas-mediated genome editing (49, 50). Potential Cas9 target guide (protospacer) sequences in the vicinity of the *Trio K1431*, *K1918*, and *M2145* codons were screened using the online tool CRISPOR (51) and candidates were selected. Templates for sgRNA synthesis were generated by PCR from a pX330 template (Addgene), sgRNAs were transcribed *in vitro* and purified (Megashortscript, MegaClear; ThermoFisher). sgRNA/Cas9 RNPs were complexed and tested for activity by zygote electroporation, incubation of embryos to blastocyst stage, and genotype scoring of indel creation at the target sites. sgRNAs that demonstrated the highest activity were selected for creating the knock-in alleles. Guide primers for generating the template for transcription included a 5' T7 promoter and a 3' sgRNA scaffold sequence and were as follows (protospacer sequence capitalized):

K1431M: 5'-tgtaatacgactcactataggACCTGATCAAACCAGTTCAGgttttagagctagaaatagc-3'

K1918X: 5'-tgtaatacgactcactataggAAGCTTCTCACGCACGCAGGgttttagagctagaaatagc-3'

M2145T: 5'-tgtaatacgactcactataggATGACATGATGAACGTCGGGgttttagagctagaaatagc-3'

Recombination template oligos (IDT) were designed to create the desired codon changes, with incorporation of silent mutations to destroy the PAM and prevent sgRNA recognition of the newly created alleles as well as create a new restriction site for genotyping. sgRNA/Cas9 RNP and the template oligo were electroporated into C57Bl/6J (JAX) zygotes (50). Embryos were transferred to the oviducts of pseudopregnant CD-1 foster females using standard techniques (52). Genotype screening of tissue biopsies from founder pups was performed by PCR amplification and Sanger sequencing to identify the desired base changes, followed by breeding and sequence confirmation to establish germline transmission of the correctly targeted alleles. Recombination template oligos were as follows (silent mutations bolded and italicized; new restriction digest site underlined):

K1431M: 5'-gccaattccatctcttcctACCTGATCAAACC***T***GT***A***CAGCG***T***ataacaa***T***gtatcagctccttttaaaggtgtgtatgaaacattgtccatctgcaacatcacaccctgtgttgatatgtatcccct-3' (creates BsrGI site)

K1918X: 5'-agctgccatctatggcaaaggcatttgtacacaggtgtgagagtgactcgcgaa***A***CT***G***CTGC***A***TGCGTGAGAAGCTTaccattttgcttt***A***cacgagttcttcaatagcactgacgagctcagctgcgctgggag-3' (creates SphI site)

M2145T: 5'-agggcccctcaataaacaatgcattacgtcaaatccctgcaG***T***CG***A***CC***A***acgttcatc***G***tgtcattacagcgcttcggcacgatgcacatgacttctacagctttctgtgggtggagagaaagca-3' (creates SalI site)

Mice were maintained on a C57BL/6J background. The mice were crossed with *thy1-GFP-M* mice (53) for visualization of individual neurons in dendritic arbor and spine analyses.

Mouse genotyping

Genotypes were determined by PCR of mouse DNA using the following primer pairs:

GFP_For: 5'-gcacgacttcttcaagtccgccatgcc-3'

GFP_Rev: 5'-gcggatcttgaagttcaccttgatgcc-3' [27]

Trio1431_For: 5'-ttgtcattaatgtggtactgtgccc-3'

Trio1431_Rev: 5'-gacaggccaagaaatgtcagtg-3'

Trio1918_For: 5'-tacgagggagttcactgtctg-3'

Trio1918_Rev: 5'-agtgcaggctatgcttcgttta-3'

Trio2145_For: 5'-gcctggacacatccgaattaga-3'

Trio2145_Rev: 5'-aataaccccggacagaggaaag-3'

To distinguish *Trio* variant and WT alleles, PCR was followed by restriction digest at 37°C for several hours (BsrGI for *K1431M*, SphI for *K1918X*, SalI for *M2145T*) and subjected to agarose gel electrophoresis. WT samples appeared as one band (530 kb for *K1431* litters, 550 kb for *K1918* litters, 400 kb for *M2145* litters); while *Trio* heterozygous variants appeared as two bands (450 and 530 kb for +/*K1431M*, 350 and 550 kb for +/*K1918X*, 350 and 400 kb for +/*M2145T*).

***In vitro* GEF Assays**

The *K1431M* point mutant was generated via site-directed mutagenesis of human WT TRIO GEF1 using the following oligos:

Oligo A: 5'-cagcgaataacgatgtatcagctcc-3'

Oligo B: 5'-ggagctgatacatcgttattcgctg-3'

WT and *+/K1431M* human TRIO GEF1 and Rac1 recombinant proteins were expressed and purified from bacteria as previously described (54). GEF activity was monitored by the decrease in fluorescent signal ($\lambda_{excitation}$ = 488 nm; $\lambda_{emission}$ = 535 nm) as BODIPY-FL-GDP was exchanged for GTP on Rac1 over 30 minutes, as previously described (47, 54).

Body weight, brain weight, and head width measurements

Mice were weighed at P42 and ear-to-ear head width was measured with calipers in anesthetized mice. Mice were decapitated and whole brains were removed from the skull. Brains were weighed at P42 after removing the olfactory bulbs and external portions of the brain stem.

Mouse brain lysate preparation

P0-P1 mice and P35-P42 brain extracts were prepared as previously described (25). Cerebella, hippocampi, and cortices were rapidly removed, snap-frozen and stored at -80°C until lysate preparation. Tissue was sonicated in homogenization buffer (1% SDS, 50 mM Tris pH 7.4, 2 mM EDTA, protease and phosphatase inhibitors (Roche 11873580001; Roche 04906837001), heated at 95° C for 5 minutes, and clarified by centrifugation; aliquots were snap frozen and stored at -80° C until immunoblotting. Protein concentrations were determined with a bicinchoninic acid (BCA) assay (Pierce).

Western blot and quantification

15 µg of brain lysate in Laemmli sample buffer (LSB) were separated on SDS-PAGE gels and transferred to nitrocellulose membrane. Membranes were stained with Ponceau S as a loading control, blocked with 5% nonfat milk in Tris-buffered saline with 0.1% Tween20 (TBS-T) for 1 h at room temperature (RT), incubated overnight at 4° C with primary antibodies (TRIO SR5-6 1:1000, (9); TRIO DH2 1:1000, (9); Munc18-1 1:1000, BDscience #bd610336; Stx1a 1:1000, (55)), then incubated at RT for 1 h with HRP-linked secondary antibodies (Bio-Rad 170-6515 and 172-1011, 1:5000), imaged via chemiluminescence on a ChemiDoc Imaging System (Bio-Rad), and analyzed in ImageJ. Signal intensity was normalized to total protein levels determined by PonceauS, then normalized again to the WT average. Measurements were compared to standards of 7.5, 15, and 30 µg protein of WT brain lysate to calibrate signal intensity versus protein level.

G-LISA assay and quantification

Active GTP-bound GTPase levels in brain lysates were measured using G-LISA activation assay kits for Rac1 (Cytoskeleton, Inc., BK128) and RhoA (Cytoskeleton, Inc., #BK124). Brains were homogenized in G-LISA lysis buffer supplemented with protease and phosphatase inhibitors (Roche), normalized to the same concentration as determined by BCA assay (Pierce), and applied to the G-LISA matrices and processed according to manufacturer's protocols. Absorbances at 490 nm (OD_{490}) were background-subtracted and normalized to the WT average.

Behavioral tests

Behavioral tests were performed in mice 6-8 weeks of age (P42-P56). Mice were habituated to handling for 5 minutes per day for 5 days prior to experiments and habituated in the test facility for at least 30 minutes prior to starting the task. We performed the Kondziela inverted screen test for motor strength, accelerating rotarod for motor coordination and learning, social preference test, novel object recognition task, open field test, elevated plus maze, and nestlet shredding, as previously described (25, 56-59).

Animal perfusion and tissue processing

Mice were transcardially perfused with heparinized PBS followed by 4% paraformaldehyde (PFA) in phosphate buffered saline (PBS). Brains were postfixed in 4% PFA at 4°C for 24 h, then stored in PBS until further processing. Fixed brains were sliced coronally at 30 µm for Nissl stain and immunohistochemistry, and 200 µm for dendritic arbor reconstructions and spine analysis. Sections were processed as per application and coverslip-mounted with ProLong Diamond Antifade Mountant (P36961, ThermoFisher).

Nissl staining

Nissl staining was performed according to standard protocols (60). Brightfield images were acquired at 20X on a SlideView VS200 slide scanner (Olympus). Sections containing the decussation of the anterior commissure were selected for analysis and quantified using QuPath software. Measurements from three consecutive slices were averaged per mouse.

Immunostaining

Desired sections were identified by comparison to a mouse brain atlas (61). Three 30-µm coronal sections from the motor cortex, spaced at 120-µm intervals and containing the rostral decussation of the corpus callosum were used for immunostaining. Mounted sections were boiled in Na-Citrate buffer (10 mM, pH 6.4) for 45 min, blocked for 1 h in 5% normal goat serum (NGS) in 0.3% PBS-T, incubated overnight at 4°C with primary antibodies (NeuN 1:1000, Synaptic Systems #26606); PV 1:1000, Swant #GP72), incubated with appropriate AlexaFluor-conjugated secondary antibodies (1:2000, Invitrogen) for 1 h at RT, and counterstained for 10 minutes with DAPI (1:10,000). Controls lacking primary antibody were used to confirm staining specificity. Fluorescent images were acquired at 10X on a SlideView VS200 slide scanner (Olympus). Semi-automatic cell counts for DAPI+, NeuN+, and PV+ stained cells were obtained using QuPath by an experimenter blinded to genotype.

Dendritic arbor reconstructions

Mice of all genotypes examined were intercrossed with mice bearing a *thy1-GFP* transgene (M line) (53). Fluorescent images of neurons contained within 200 µm coronal sections were acquired at 20X on a Zeiss LSM900 confocal laser scanning microscope. L5 PNs with an intact apical dendrite in the M1 motor cortex were identified by comparison to a mouse brain atlas (61). Z-stack images were acquired and exported to ImageJ (NIH), and dendrites were traced using the Simple Neurite Tracer Fiji plugin (SNT). Sholl analysis, measurements of dendrite length and branching, convex hull analysis, and path length analysis were measured from these traces in SNT.

Dendritic spine density analysis

L5 PNs within 200 µm coronal slices of *thy1-GFP* -labeled dendrite arbors were imaged at 100x on an UltraVIEW VoX spinning disc confocal (Perkin Elmer) Nikon Ti-E-Eclipse microscope. Full z-stack images were merged in ImageJ. Dendritic spines were manually counted on secondary apical and basal dendritic branches by an experimenter blinded to genotype.

Electron microscopy

Electron microscopy of synapses in M1 layer 5 was performed as previously described (25). Measurements of synapse density, PSD length, spine head area, presynaptic bouton area, and synaptic vesicle (SV) distribution were quantified in ImageJ as previously described (62, 63) from 5-18 fields of view (~50 μm^2) per mouse.

Electrophysiological recordings

Acute slices were prepared from mice at P35-42 as previously described (25) with minor modifications noted here. Coronal slices of M1-M2 cortex were cut at 360 µm in ice-cold N-Methyl-D-glucamine-aCSF (NMDG-aCSF, in mM): 120 NMDG, 2.5 KCl, 7 $MgSO_4$, 1.25 NaH_2PO_4, 0.5 $CaCl_2$, 28 $NaHCO_3$, 13 glucose, 7 sucrose, saturated with 95% O2-5% O2 at 300-320 mOsmol/L, pH 7.4) on a vibratome (Leica) and recovered in normal ACSF at 32ºC for 30 minutes followed by 1 h recovery at RT. Recorded signals were low pass filtered at 4 kHz and digitized at 8 kHz with a Digidata 1440 digitizer (Molecular Devices). Cells were excluded if series resistance changed >20%. Data were collected in pClamp 11.1 and analyzed with Clampfit 11.1.

Excitatory postsynaptic currents (EPSCs) were evoked (e) by a tungsten bipolar stimulating electrode placed in M1 L2/3 with stimulus intensities that yielded 40%–50% of the maximal response. AMPAR-eEPSC amplitudes were measured at the peak of the EPSC recorded at -70 mV holding potential. N-methyl-D-aspartate NMDAR-eEPSC amplitudes were recorded

from the same neurons at +40 mV and measured at 40 ms after the stimulus artifact when AMPAR-eEPSCs have decayed.

Miniature EPSCs (mEPSCs) were recorded in whole-cell patch mode. AMPAR-mEPSCs were recorded at -70 mV and NMDAR-mEPSCs were recorded at +40 mV with tetrodotoxin and bicuculline methiodide (BMI) in the external solution, gamma-aminobutyric acid receptor and glycine receptor inhibitory postsynaptic currents (GABAR/GlyR-mIPSCs) were recorded at +15 mV. Amplitude and frequency of miniature events were detected using Mini-Analysis software (Synaptosoft, Decatur, GA) and inspected visually.

Paired-pulse stimulation was applied with interstimulus intervals (ISIs) of 35, 60, 100, 200 or 300 ms. The amplitude of the second eEPSC ($EPSC_2$), evoked by the second of the paired-pulse stimulations, was divided by $eEPSC_1$ amplitude to obtain a paired-pulse ratio (PPR). Long-term potentiation (LTP) of evoked EPSCs (recorded at -70 mV) was induced by theta-burst stimulation (TBS, five trains of four pulses at 100 Hz in 200 ms intervals, repeated four times with an interval of 10 s) in the presence of 10 μM BMI.

Estimations of the readily releasable pool (RRP) size and synaptic vesicles (SVs) depletion rate were made from recordings of AMPAR-eEPSCs using high frequency stimulation (HFS, 40Hz) trains of 15 pulses to deplete the RRP. RRP recovery was approximated as fractional recovery using initial train stimulation with interstimulus intervals of 0.1, 2, 5, and 10 s, followed by the single stimulus. Fractional recovery for each ISI was calculated as (eEPSCs2-eEPSCt1ss)/(eEPSCt1-eEPSCt1ss), where eEPSCs2-amplitude of the stimulus applied after the train, eEPSCt1-first amplitude of the train, eEPSCt1ss-steady state amplitude of the train (last 5-6 responses). 1 mM kynurenic acid was added to prevent AMPA receptor saturation; 50 μM D-2-Amino-5-phosphonovaleric acid (D-AP5) and 20 μM BMI were added to block NMDA receptors and GABA receptors, respectively. Trains were analyzed to estimate glutamate probability of release (Pr) and RRP for each neuron as previously described (64, 65) using OriginLab 9 software.

Data Analysis

Statistical analyses were performed using GraphPad Prism 10. Data in bar graphs are presented as mean ±SEM, with individual data points graphed when applicable. Sample size 'n' is annotated within the bars or in the figure legend for each group. Distributions were tested for normality and outliers were removed before proceeding with statistical tests. Specific details of statistical tests performed, adjusted with post-hoc Bonferroni test for multiple comparisons (MC) where appropriate, are included in the figure legends. Significance was defined by a p-value less than 0.05: $^{ns}p<0.1$; $*p<0.05$; $**p<0.01$; $***p<0.001$; $****p<0.0001$.

RESULTS

Generation of *Trio* variant mice and impact on *Trio* isoforms

We used CRISPR/Cas9 technology to generate mice bearing heterozygous *Trio* rare variant alleles associated with ASD (*+/K1431M*) and SCZ (*+/K1918X*), and a *de novo* mutation found in an individual with BPD (*+/M2145T*) **(Fig. 1A,B)**. We chose these alleles for their discrete, measurable effects on TRIO levels or activity: *K1431M* impairs TRIO GEF1 activity up to 8-fold **(Supp. Fig. 1A,B)** (9), *M2145T* increases GEF2 activity 4-fold (9), and *K1918X* creates a premature stop codon between GEF1 and GEF2.

Mice heterozygous for these *Trio* alleles survived to adulthood. Mice homozygous for *Trio K1431M* and *M2145T* survived to adulthood, with *K1431M* litters observed in expected Mendelian ratios and fewer *M2145T* homozygotes than expected **(Supp. Fig. 1C)**. *K1918X* homozygote pups were not observed, as expected for a *Trio* null allele (22, 24). We focused on analysis of heterozygotes, as most rare damaging *Trio* variants are heterozygous in humans. Heterozygosity for the *K1431M* and *M2145T* alleles did not significantly alter Trio protein levels in the neonate mouse brain at postnatal day 0 (P0) **(Fig. 1C-D)**, nor did these alleles alter relative levels of the predominant Trio isoforms in the P42 adult mouse brain: Trio9 (Trio9S 263 kDa; Trio9L 277 kDa) and Duet (145 kDa) throughout the brain, and Trio8 in the cerebellum (217 kDa) (11, 12) **(Fig. 1A, Supp. Fig. 1D-L)**. We did not detect a signal corresponding to the predicted size of a truncated protein resulting from *K1918X* mutation (217 kDa) in *+/K1918X* mice, suggesting instead that this mutation leads to nonsense-mediated decay. Consistent with this, Trio9 protein levels were reduced by ~50% in the brains of *+/K1918X* mice at P0 **(Fig. 1C-D)** and at P42 **(Supp. Fig. 1D-L)**, consistent with the introduction of a stop codon into a key exon of this isoform; however, levels of the other abundant Trio isoforms present in the adult mouse brain, Trio8 and Duet, were unaffected **(Supp. Fig. 1D-L)**.

Trio variant alleles differentially impact active Rho family GTPase levels.

Given the effects of these variants on TRIO GEF activity *in vitro*, we measured levels of active GTP-bound Rac1 and RhoA in brains of neonatal (P0) and adult (P42) *Trio* variant-bearing mice via an ELISA-based assay **(Fig. 1E-H)**. In concordance with the ~50% reduction in Trio levels in *+/K1918X* brains, we found decreased active Rac1 in P0 *+/K1918X* brains (91% of WT activity), with no significant changes in active RhoA levels. By P42, *+/K1918X* brains did not differ from WT in Rac1 or RhoA activity.

As *K1431M* decreases TRIO GEF1 catalytic activity *in vitro* **(Supp. Fig. 1A,B),** we anticipated Rac1 levels might be reduced in *+/K1431M* mice (9, 26, 33). Instead, GTP-bound Rac1 levels were increased in *+/K1431M* whole brain lysates compared to WT controls at P0 (111% of WT) and even higher at P42 (150% of WT). Despite the increased GEF2 activity

mediated by M2145T TRIO (9), we did not detect changes in active RhoA levels in *+/M2145T* mouse brain at either age.

Distinct *Trio* variants differentially impact mouse behavior.

NDDs affect learning and memory, compulsivity, motor development and coordination, and social skills. We used a battery of behavioral tests to assess these skills in mice bearing *Trio* variants.

We measured motor coordination and learning using an accelerating rotarod test. *+/K1431M* and *+/K1918X* mice of both sexes fell from an accelerating rotarod with reduced latency and improved more slowly in this skill over repeated trials relative to WT littermates **(Fig. 2A)**, while *+/M2145T* mice performed similarly to WT. No deficits in muscle strength were noted in any genotype using the Kondziela inverted screen test prior to rotarod testing, and no differences in general locomotor activity or exploratory behavior were seen in an open field test **(data not shown)**.

Individuals with ASD exhibit deficits in social interactions (1). In a three-chamber social interaction test, *+/K1431M* mice of both sexes showed no preference for the stranger mouse over the object **(Fig. 2B)**. *+/M2145T* mice of both sexes and *+/K1918X* males exhibited normal social preference similar to WT.

Recognition memory is impaired in individuals with SCZ (66, 67). In a novel object recognition test, *+/K1918X* mice of both sexes and *+/M2145T* females failed to discriminate between the novel and familiar objects, while *+/K1431M* mice and *+/M2145T* males exhibited normal discrimination between novel and familiar objects similar to WT **(Fig. 2C)**.

Repetitive behaviors and motor stereotypies are key features of ASD and SCZ (68). We found that *+/K1918X* males exhibited significantly more compulsive nestlet shredding relative to WT, while *+/K1431M* males showed a trend toward increased nestlet shredding **(Fig. 2D)**.

Overall, we observed overlapping behavioral phenotypes between *+/K1431M* and *+/K1918X* mice, though there were distinct differences particularly in social interaction and memory tests. *+/M2145T* mice exhibited the fewest phenotypes in the tasks measured here. Together, these data strongly suggest that these *Trio* alleles differentially impact behavior.

***Trio +/K1431M* and *+/K1918X* mice have smaller brains.**

TRIO variants that reduce TRIO GEF1 activity are associated with microcephaly (29, 30, 47), so we assessed head and brain size in *Trio* variant mice **(Fig. 3A,B, Supp. Fig. 2A-C)**. After adjusting for body weight, both the head width-to-body weight ratio and brain-to-body weight ratio **(Fig. 3A,B)** were reduced in adult *+/K1431M* mice relative to WT, consistent with the microcephaly seen in patients harboring *TRIO* GEF1-deficient alleles. Reduced head width in *+/K1918X* mice was in proportion to their body weight (head width-to-body weight ratios did

not differ between *+/K1918X* and WT mice, p>0.95). However, *+/K1918X* mice still displayed a reduced brain-to-body weight ratio relative to WT, suggesting a disproportionate reduction in brain mass relative to their already smaller head size. Meanwhile, *+/M2145T* mice did not differ from WT in either head width or brain weight when normalized to body weight.

***Trio* variant mice show minimal changes in cortical organization.**

We examined whether the decreased brain weight and head size observed in *+/K1431M* and *+/K1918X* mice were associated with anatomical defects. Histological analyses of fixed Nissl-stained brain sections did not reveal gross morphological defects **(data not shown)**. We observed reductions in both total cross-sectional brain area and cortical thickness in *+/K1918X* brains **(Fig. 3C-E)**, consistent with their smaller head size and brain weight. Significant decreases in cortical layer 2/3 and layer 5 thickness were observed in *+/K1918X* brains; but these were in proportion to the relative decrease in cortical thickness as compared to WT **(Supp. Fig. 2D,E)**.

We found no differences in total cortical cell density or in layer-specific cell density in *Trio* variant mice relative to WT, nor were numbers or proportions of cortical NeuN+ neuronal cells or PV+ inhibitory neurons altered relative to WT **(Supp. Fig. 2F-N)**, suggesting the reduced brain size was instead due to loss of neuropil.

***Trio* variant heterozygotes exhibit alterations in dendritic arbors and synaptic ultrastructure.**

Altered dendritic arbor morphology and dendritic spine abnormalities are hallmarks of NDDs (69-75); for instance, spine density is greater in ASD and decreased in SCZ and BPD (76-79). Prior work showed that excitatory neuron-specific ablation of one or both *Trio* alleles decreased dendritic arborization, increased dendritic spine density, and yielded smaller, less efficacious synapses in cortex area M1 Layer 5 pyramidal neurons (M1 L5 PNs) (25).

Sholl analysis of M1 L5 PNs revealed a significant reduction in both basal and apical dendritic arbor complexity and dendritic field size in P42 *+/K1918X* neurons, a modest increase in proximal basal arbor complexity in *+/K1431M* neurons, and a very slight decrease in distal apical arbor complexity in *+/M2145T* neurons relative to WT **(Fig. 3F-H, Supp. Fig. 3A,B)**. Corresponding changes in branch number and branch length were not apparent when all dendrites were aggregated for analysis **(Supp. Fig. C-H)**, but path length analysis revealed that branch numbers were increased for lower order dendrites in *+/K1431M* neurons, while average branch lengths were decreased at higher order dendrites in *+/K1918X* neurons (**Supp. Fig. 3I-N)**.

Dendritic spine density and morphology determine overall neuronal connectivity and the strength and stability of excitatory synaptic transmission (80-82). None of the *Trio* variant

heterozygotes exhibited altered dendritic spine density on M1 L5 pyramidal neurons compared to WT mice **(Fig. 3I,J**), either on apical or basal arbors.

We used electron microscopy to enumerate synapses and measure their dimensions in cortical area M1 L5. Synapse density was significantly increased in *+/K1918X* mice **(Fig. 4A,B)**, possibly due to a net reduction in neuropil resulting from smaller dendritic arbors. Cross-sectional presynaptic bouton area and spine head area were similar to WT in each *Trio* variant heterozygote **(Fig. 4D,E)**. Within synapses, postsynaptic density (PSD) length was slightly decreased in *+/K1918X* and *+/M2145T* mice, but not in *+/K1431M* mice **(Fig. 4C)**.

We also measured synaptic vesicle (SV) distribution as a function of distance from the active zone (AZ). SV distribution within 15-150 nm from the AZ, which is believed to include the readily-releasable pool (RRP), were significantly increased in *+/M2145T* mice relative to the other genotypes **(Fig. 4F,G)**. Vesicles at 200 nm from the AZ were also significantly increased in *+/M2145T* and mice, suggesting an overall larger SV pool size **(Fig. 4G)**. No differences in synaptic vesicle distribution were noted in *+/K1431M* mice, while *+/K1918X* showed modestly increased SVs at 200 nm from AZ relative to WT.

Synaptic transmission and plasticity are differentially impaired by distinct *Trio* variants.

Loss of Trio function or disruption of TRIO GEF1 activity in slice culture decreases AMPAR levels at excitatory synapses (25, 27, 28, 33); meanwhile mice bearing a GEF1-deficient *Trio* allele exhibited decreased gamma-aminobutyric acid receptor (GABAR)- and glycine receptor (GlyR)-mediated inhibitory miniature current (mIPSC) frequencies in the prefrontal cortex (26). To explore how *Trio* variants impact synaptic function, we measured both miniature excitatory currents (mEPSCs) and mIPSCs in M1 L5 PNs in each of the Trio variant heterozygotes. AMPAR-mediated mEPSC amplitudes were significantly increased in *+/K1431M* and *+/K1918X* mice relative to WT littermates, with no change in their frequencies **(Fig. 5A-C)**. In contrast, AMPAR-mediated mEPSC amplitudes were unchanged in *+/M2145T* mice, but their frequencies were significantly increased **(Fig. 5A-C)**. No significant changes in NMDAR-mediated mEPSC amplitudes were noted, although *+/M2145T* mEPSCs exhibited a trend toward increased frequency **(Fig. 5D-F)**. Notably, these findings correlated with gross alterations in the ratio of NMDAR/AMPAR-mediated evoked (e)EPSCs measured in M1 L5 PNs following stimulation in L2/3. All *Trio* variant heterozygotes showed decreased NMDA/AMPA ratios, indicating general imbalances in NMDAR- versus AMPAR-mediated conductance **(Supp. Fig. 4A,B)**.

Given that Trio is expressed in both excitatory and inhibitory neurons, we recorded mIPSCs onto M1 L5 PNs. Significant decreases in mIPSC frequencies were noted in *+/K1431M* and *+/M2145T* mice relative to WT mice, with no change in amplitudes **(Fig. 5G-I)**. *+/K1918X* mice exhibited increased mIPSC amplitude with no observed change in mIPSC frequency **(Fig. 5G-**

I). Together, these data indicate that the *Trio* variants differentially impact excitatory and inhibitory transmission.

Finally, given these impairments in excitatory and inhibitory transmission, we tested the ability of the L5 PNs to undergo LTP following theta-burst stimulation of L2/3 afferents. While LTP was robustly induced and potentiated in M1 L5 PNs from WT mice, LTP induction and potentiation were deficient in slices from *+/K1918X* and *+/K1431M* mutant mice **(Fig. 5J,K)**. In contrast, *+/M2145T* L5 PNs showed increased induction and prolonged potentiation of LTP compared to WT L5 PNs **(Fig. 5J,K)**.

Neurotransmitter release is altered in *Trio +/K1431M* and *+/M2145T* heterozygotes.

In addition to regulating postsynaptic responses, Trio localizes presynaptically and interacts with the presynaptic active zone scaffolding proteins Bassoon and Piccolo (28, 43, 44). To assess the impact of *Trio* variants on presynaptic function, we first measured the paired-pulse ratio (PPR). Synapses with low probability of release (Pr), such as those formed by L2/3 onto L5 PNs, can undergo paired-pulse facilitation (PPF), a relative increase of synaptic transmission in response to the second of two closely-apposed stimuli. WT and *+/K1918X* M1 L5 PNs exhibited normal facilitation of eEPSC amplitudes that decreased with increased interstimulus interval (ISI) **(Fig. 6A,B)**. PPF was significantly enhanced in *+/K1431M* M1 L5 PNs at short ISIs relative to WT, suggesting a possible reduction in glutamate Pr **(Fig. 6A,B).** The *+/M2145T* PPR curve was unusual, with significantly reduced PPF at short ISIs, yet clear PPF increase at longer ISI **(Fig. 6A, B)** compared to WT. The decreased PPF at initial ISI in *+/M2145T* mice correlated with increased mEPSCs frequency **(Fig. 5A-C)**, suggestive of a possible increase in glutamate Pr.

We next used high frequency (40Hz) stimulation (HFS) trains to quantitatively estimate glutamate Pr, RRP size, and rates of SV depletion and recovery. A plot of the HFS train normalized eEPSC responses again revealed facilitation upon the first 2-3 stimulations that was increased in *+/K1431M* and decreased in *+/M2145T* slices relative to WT, with no changes in *+/K1918X* (**Fig. 6C,D**). This initial facilitation was followed by decaying eEPSC amplitudes, reflecting SV depletion under HFS. All *Trio* variants exhibited a slower train decay rate relative to WT during HFS (τ_d, 4.8 s vs WT: 2.7 s) with *+/M2145T* depleting at half the rate of WT **(Fig. 6D)**.

We used a 'Decay' method (64, 65), which accounts for initial facilitation of the first responses in the train at low probability synapses, to quantitatively estimate Pr and RRP size from HFS trains. Glutamate Pr in the L2/3-L5 synapses was increased in *+/M2145T* mice, while it was decreased for *+/K1431M* mice **(Fig. 6F)**, consistent with the relative changes observed in PPF for these mice. RRP size was much larger in L2/3-L5 synapses of *+/M2145T* mice relative to WT **(Fig. 6J)**, consistent with the increased SV distribution found in close

apposition to the AZ **(Fig. 5G,F)**. We tested the ability of the *Trio* variant heterozygotes to recover after train depletion by pairing HFS trains at increasing intervals between trains (0.01, 2, 6, 9, 12, 18s). The recovery rate (τ_R) was significantly slower in *+/K1431M* L5 PNs and they did not recover to their initial strength within 18s, plateauing at 78% of maximal recovery compared to WT **(Fig. 6K)**. This modeled increase in glutamate Pr in *+/M2145T* slices was consistent with the measured increase in AMPAR mEPSCs frequency; even while no changes in dendritic spine density were observed in these mice.

Given our findings, we investigated whether the *Trio* variants might impact presynaptic regulators, including Munc18-1 and Stx1a, which are crucial for synaptic vesicle (SV) docking, and replenishment respectively. Quantitative immunoblotting of cortical lysates revealed a significantly increased level of Munc18-1 and Stx1a in *+/M2145T* lysates and decreased levels of both in *+/K1431M*, with no significant changes *+/K1918X* (data not shown) compared to WT mice (**Fig. 6L-N**). Together, our data indicates robust presynaptic alterations at L2/3-L5 synapses in *+/K1431M* and *+/M2145T* mice, that are driven by deficits in levels of Munc18-1 and Stx1a, presynaptic regulatory proteins, with no dramatic changes in *+/K1918X*.

DISCUSSION

While autism, schizophrenia, and bipolar disorder are recognized clinically as distinct disorders, large-scale genetic studies show significant overlap in risk genes for multiple NDDs, many converging on synaptic proteins (4, 83-90). However, how mutations in a single gene can contribute to different NDDs remains a major unresolved question. In this study, we generated three new mouse models harboring variants in *Trio* found in patients with ASD (*+/K1431M*), SCZ (*+/K1918X*), and BPD (*+/M2145T*). Our study demonstrates that heterozygosity for these variants, which differentially affect Trio protein levels or GEF activity, yield overlapping but distinct phenotypes at the behavioral, neuroanatomical, and synaptic levels. Our findings extend prior work demonstrating that Trio is critical for postsynaptic signaling and synaptic plasticity. We also demonstrate for the first time that Trio is critical for glutamate release and synaptic vesicle recycling, and that NDD-associated variants differentially impact these pre- and post-synaptic roles.

Heterozygosity for *Trio* variants in mice reflects phenotypes observed in patients with NDDs

Individuals with mutations in *TRIO* present with a range of neurodevelopmental disorder-associated clinical features, including varying degrees of intellectual disability, altered head size, skeletal and facial features, and behavioral abnormalities such as autistic tendencies, attention deficits, learning difficulties, motor stereotypies, hyperactivity, and anxiety (8, 29-32, 47, 91). Patients with missense or truncating variants in *TRIO* that reduce GEF1 activity have mild developmental delay and microcephaly (29, 30, 32, 47). Similarly, we found that mice heterozygous for the GEF1-deficient *K1431M* missense mutation or the *+/K1918X* nonsense mutation, which reduced overall Trio levels, had significantly reduced brain weight and/or head size compared to WT mice, along with multiple behavioral impairments. Notably, while both showed impaired motor coordination and learning, only mice bearing the ASD-associated *K1431M* allele exhibited social interaction deficits while *+/K1918X* mice were normal in this regard.

Both *+/K1431M* and *+/K1918X* adult mice had reduced brain-to-body weight ratios compared to WT, but driven by different factors. The smaller brain size in *+/K1918X* mice was associated with a reduction in neuropil and reduced cortical thickness, similar to what was previously observed in mice bearing excitatory neuron-specific ablation of one *Trio* allele (25), and reflecting findings of reduced gray matter volume and cortical thickness in neuroimaging studies of patients with schizophrenia (92-96). Meanwhile, we found that *+/K1431M* mice had no change in neuropil or cross-sectional brain area, consistent with a prior study describing normal brain size in *+/K1431M* and *K1431M/K1431M* mice at E14.5 (26).

Furthermore, we observed an overall *decrease* in body weight of *+/K1918X* males and an *increase* in body weight in *+/K1431M* mice compared to WT, which drove the reductions in head width- and brain-to-body weight ratios. Rac1 activity is well known to play a functional role in metabolism, particularly by mediating glucose-stimulated insulin secretion from pancreatic islet beta-cells (97-102), so it is not surprising that chronic alterations in Rac activity may contribute to weight changes in *Trio +/K1431M* and *+/K1918X* mice. While most studies of specific *Trio* variants have focused on neuronal effects, expression of *Trio* in other tissues may explain the body weight changes observed in these mice, as well as the musculoskeletal abnormalities associated with *TRIO* variation in humans (8, 29, 31, 46).

Effect of *Trio* variants on dendrites

Based on the effects of Rac1 and RhoA signaling on the neuronal actin cytoskeleton (13, 39-42), we hypothesized that *Trio K1431M*, *K1918X*, and *M2145T* variants would significantly impact dendritic arbor branching and length. Instead, the *Trio* variants had relatively subtle effects on cortical L5 PN dendrites. The reductions in dendritic arborization and length in *+/K1918X* neurons are consistent with reports of reduced gray matter volume and dendrite alterations in individuals with schizophrenia versus controls (103, 104), but were quite modest compared to *NEX-Trio*$^{+/fl}$ mice lacking one copy of Trio in excitatory neurons (25). Reduced Trio function in other cell types, such as in inhibitory neurons or glia, or in neurons from other brain regions that project to cortical M1 L5 PNs, may ameliorate the phenotypes in excitatory neurons of *+/K1918X* relative to *NEX-Trio*$^{+/fl}$ mice. In addition, changes to L5 PN dendrites in *Trio* variant mice appeared to be regionally selective within the arbor: *+/K1431M* neurons had increased arborization only in proximal basal dendrites, while *+/M2145T* neurons had decreased arborization only in the most distal apical dendrites. These differences may reflect the differential spatiotemporal influence of Trio in regulating Rac1 versus RhoA activity. Alternatively, given our finding for presynaptic roles for Trio, these differences may reflect differential effects of the *Trio* variants on both excitatory and inhibitory afferent synaptic inputs to the apical versus basal dendrites of L5 PNs (105) , which play critical roles in shaping the arbors.

***Trio* variants only modestly impact brain Rho GTPase signaling, yet in unexpected ways.**

We show here that the *K1431M* mutation within the TRIO GEF1 domain significantly reduces nucleotide exchange on Rac1, consistent with previous reports (9, 33). Unexpectedly, levels of active Rac1 were increased in *+/K1431M* neonatal whole brain lysates, and this became more pronounced in adult mice. This increase in Rac1 activity in *+/K1431M* brains may explain why we did not observe changes anticipated from reduced Rac1 activity in these mice, such

as reductions in brain volume, dendrites and spines, or AMPAR signaling. Sun et al (26) reported a gene dose-dependent decrease in Rac1 activity in *+/K1431M* and *K1431M/K1431M* mice at E14.5 in the ganglionic eminence, which is enriched for GABAergic interneurons. In contrast, we measured active Rac1 levels in the whole brain, where the majority of neurons are excitatory and there is a substantial glial population. We propose that the increased Rac1 activity in *+/K1431M* mouse cortex may reflect some homeostatic compensation in Rac1 regulation occurring between birth to adult ages, but the underlying mechanism is unclear.

Despite only having ~50% of WT levels of Trio, *+/K1918X* mice displayed relatively modest effects on Rho GTPase activity in the brain, with a ~10% decrease in Rac1 activity (and a non-significant trend toward decreased RhoA activity) in neonates, and notably no differences from WT in adults. Likewise, we did not observe any changes in RhoA activity in *+/M2145T* mouse cortex despite this mutation increasing *TRIO* GEF2 activity *in vitro.* Again, this lack of change in activity may reflect compensatory mechanisms that normalize Rac1 and RhoA signaling. Of the many GEFs and GAPs expressed in the brain, TRIO may regulate Rac1 and/or RhoA only within a precise spatiotemporal window or within a narrowly defined subcellular context (16, 38, 106, 107). Further studies measuring local Rac1 and RhoA activity, either in subcellular fractions or by using activity-based reporters in cells, may help to resolve where and when Trio might act to regulate Rac1/RhoA and possible compensatory responses in these *Trio* mutants. It is also possible that Trio GEF1 and GEF2 act via other unknown GTPase substrates.

The NDD-associated *Trio* variants cause diverse signaling aberrations, altered LTP, and E/I imbalance.

Overexpression of a TRIO variant with reduced GEF1 activity decreased AMPAR-mediated mESPC amplitudes in rat organotypic slices (108), while Rac1 activation increased AMPAR amplitudes by promoting synaptic AMPAR clustering (109). In notable contrast to overexpression studies, we observed increased AMPAR current amplitudes in *+/K1431M* mice, without significant changes in NMDAR-mediated mESPC amplitudes, consistent with the increased active Rac1 levels measured in adult *+/K1431M* brain extracts. AMPAR-mediated mEPSC amplitudes were also increased in *+/K1918X* L5 PNs despite no detectable change in Rac1 or RhoA activity. As noted above, it remains possible that localized changes in Rac1 activity drive the increased AMPAR tone, but are not detectable by measuring Rac1 levels in whole brain extracts.

mIPSC frequencies were decreased in both *+/K1431M* and *+/M2145T* L5 PNs. Sun et al. noted a similar deficit in inhibitory function in *+/K1431M* prefrontal cortex, which correlated with reduced interneuron migration to this region, including parvalbumin positive (PV+)

neurons (26). However, we did not observe reduced PV-positive interneuron numbers in the motor cortex in any *Trio* variant mice. Our observations suggest that in addition to regulating neuronal migration, the *K1431M* and *M2145T* can directly impact inhibitory neurotransmission. We also detected a significantly increased mIPSC amplitude in *+/K1918X* motor cortex, suggestive of a wholesale change in inhibitory tone. Together, our data indicate that heterozygosity of *Trio* variants in vivo lead to dysregulation of excitatory and inhibitory synaptic transmission in different patterns, resulting in E/I imbalance, known to be a driver of NDD phenotypes.

Trio-deficient excitatory neurons are unable to undergo long-term potentiation (LTP) in mouse brain slices (25), which is crucial for working memory in mammals. Notably, Rac1 has important roles in LTP: transient Rac1 activation increases synaptic AMPAR clustering required for LTP induction, while Rac1 inactivation is required for LTP maintenance (110-112). Both *+/K1431M* and *+/K1918X* L5 PNs exhibited deficiencies in LTP induction. The increased Rac1 activity and increased AMPAR amplitudes in *+/K1431M* slices may preclude further LTP. It is less clear why LTP is impaired in *+/K1918X* mice. One possibility is that the increased mIPSC amplitude and corresponding elevated inhibitory tone may limit LTP induction. *+/M2145T* showed a striking increase in the induction and maintenance of LTP, correlating with an increase in glutamate Pr and SV pool size measured in these mice.

Trio GEF1-deficient and GEF2-hyperactive variants lead to opposing defects in synaptic release of glutamate.

In non-neuronal systems, Trio GEF1 activity, Rac1 and RhoA are all required for regulated exocytosis in neuroendocrine, pancreatic beta, and mast cells (113-117). We present evidence here that Trio plays key roles in regulating neurotransmitter release and synaptic vesicle cycling. Several recent studies suggest that Trio may act via Rac1 and RhoA to regulate these processes – Rac1 co-localizes with SVs in the neuronal pre-synaptic compartment, where it negatively regulates glutamate Pr and SV replenishment (118-120). Hence, elevated Rac1 activity in *+/K1431M* mice may be driving the deficiencies in glutamate Pr and reduced SV replenishment. Inhibition of RhoA signaling through ROCK decreases glutamate Pr in rat brainstem motor neurons and hippocampal cultures (63, 121). Although we did not detect wholesale changes in RhoA activity in brain extracts of *+/M2145T* mice, it is possible that localized increases in RhoA activity, undetectable at a whole brain extract level, may underlie the increased Pr and SV pool size in these mice. We note that *+K1431M* mice exhibit reductions and *+/M2145T* mice exhibit increases of Stx1a and Munc18-1. Given their crucial roles in SV recycling, priming, and docking (122-125), these changes may underlie the deficits and enhancements in Pr and SV pool in *+K1431M* and *+/M2145T* mice, respectively.

At present, the molecular events that link altered Trio GEF1 or GEF2 activity to altered Stx1a and Munc18-1 levels are unclear.

Conclusions

TRIO is a risk gene for several NDDs with different patterns of variants observed in different disorders. We show here that variants in *Trio* that lead to impaired Trio levels or GEF function cause both shared and distinct defects in behavior, neuroanatomy, and synaptic function that reflect variant-specific NDD clinical phenotypes. Our data also demonstrate, for the first time, the differential impact of distinct *Trio* lesions on glutamate Pr and SVs replenishment, along with alterations in presynaptic release machinery that contribute to these deficits. We propose that distinct Trio variants act via diverse mechanisms to disrupt normal brain function at the synaptic, circuit, and behavior level.

ACKNOWLEDGEMENTS

We are grateful to Xianyun Ye, Suxia Bai, Andrew Boulton, Chris Kaliszewski, and Xiao-Yuan Li for expert technical support and Bruce Herring, Dick Mains and Betty Eipper for formative discussions.

AUTHOR CONTRIBUTION

YI, ATJ and AJK designed the study and wrote the manuscript. ATJ, AJK, and TN designed alleles and CRISPR strategy and screened pups for germline transmission. TN and the Yale Genome Editing Center generated *Trio* CRISPR alleles. YI conducted and analyzed all electrophysiology experiments. ATJ conducted dendrite reconstructions, dendritic spine analysis, and brain and body weight experiments. SF performed and analyzed all behavioral tests. ATJ collected samples; CMR, KN, and SAM measured protein levels in brain tissue. EEC perfused animals, CAG provided support, and ATJ and YI analyzed images from electron microscopy experiments. YI and ATJ conducted immunoblots and analysis. ATJ conducted Nissl stain and fluorescent immunohistochemistry; ATJ and MJV performed IHC analysis. MGC conducted GEF assays.

CONFLICT OF INTEREST

Authors declare no conflict of interest.

FIGURES

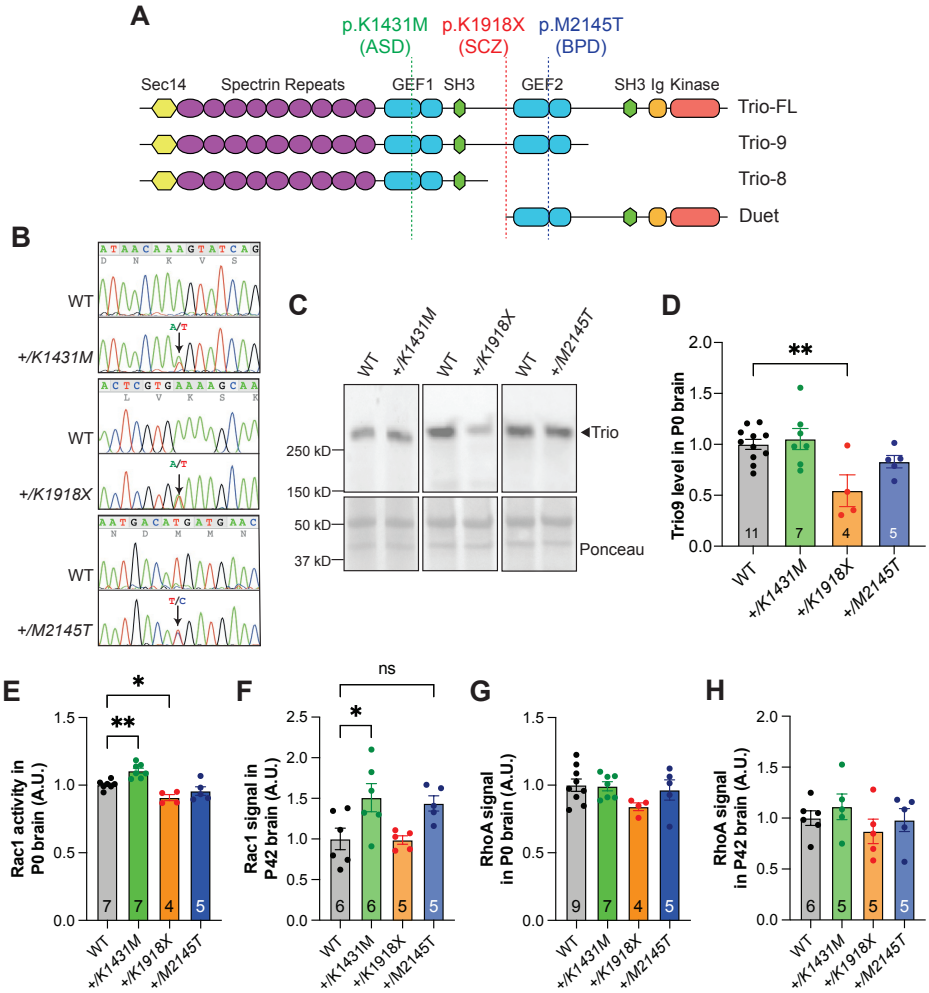

Fig. 1. Genetically engineered mice with heterozygosity for *K1431M*, *K1918X*, or *M2145T* *Trio* variants have divergent effects on Trio protein expression and Rho GTPase activity.

(A) Schematic of major Trio isoforms present in the adult mouse brain, with locations of engineered NDD-associated *Trio* variants: *K1431M* ASD-associated missense variant in the GEF1 DH domain; *K1918X* SCZ-associated nonsense variant that lies just before the GEF2 domain; and *M2145T* BPD-associated missense variant in the GEF2 DH domain. **(B)** Representative sequencing chromatograms of wild-type (WT), *+/K1431M*, *+/K1918X*, and *+/M2145T* mice. Arrows indicate heterozygosity for the variant alleles. **(C)** Representative immunoblots for Trio in P0 brain lysates using an antibody against Trio spectrin repeats (SR5-6). **(D)** Quantification of Trio protein levels from P0 brain lysates. Trio protein levels are reduced only in the brains of *+/K1918X* mice compared to WT controls (0.545 ±0.126 of WT level, p=0.0046). **(E-H)** Activity levels of Rac1 (**E,F**) and RhoA (**G,H**) in whole brain homogenates of neonate (P0) and adult (P42) *Trio* variant mice as measured by G-LISA

assay. Rac1 activity is increased in *+/K1431M* mice relative to WT at both ages (1.106 ±0.027-fold at P0, p=0.0035; 1.509 ±0.175-fold at P42, p=0.0279) and decreased in neonate *+/K1918X* mice (0.908 ±0.0.032-fold, p=0.0230), with a trend towards increased activity in adult *+/M2145T* mice (1.438 ±0.183-fold, p=0.0843); meanwhile RhoA activity appears unchanged in all mice relative to WT, though there may be a trend towards decreased activity in *+/K1918X* neonates (0.840 ±0.074-fold, p=0.1292). Data are presented as mean ±SEM. One-way ANOVA with post-hoc Bonferroni MC test identified differences from WT (^{ns}p<0.1, *p<0.05, **p<0.01). Numbers of mice quantified per group are annotated inside the bar.

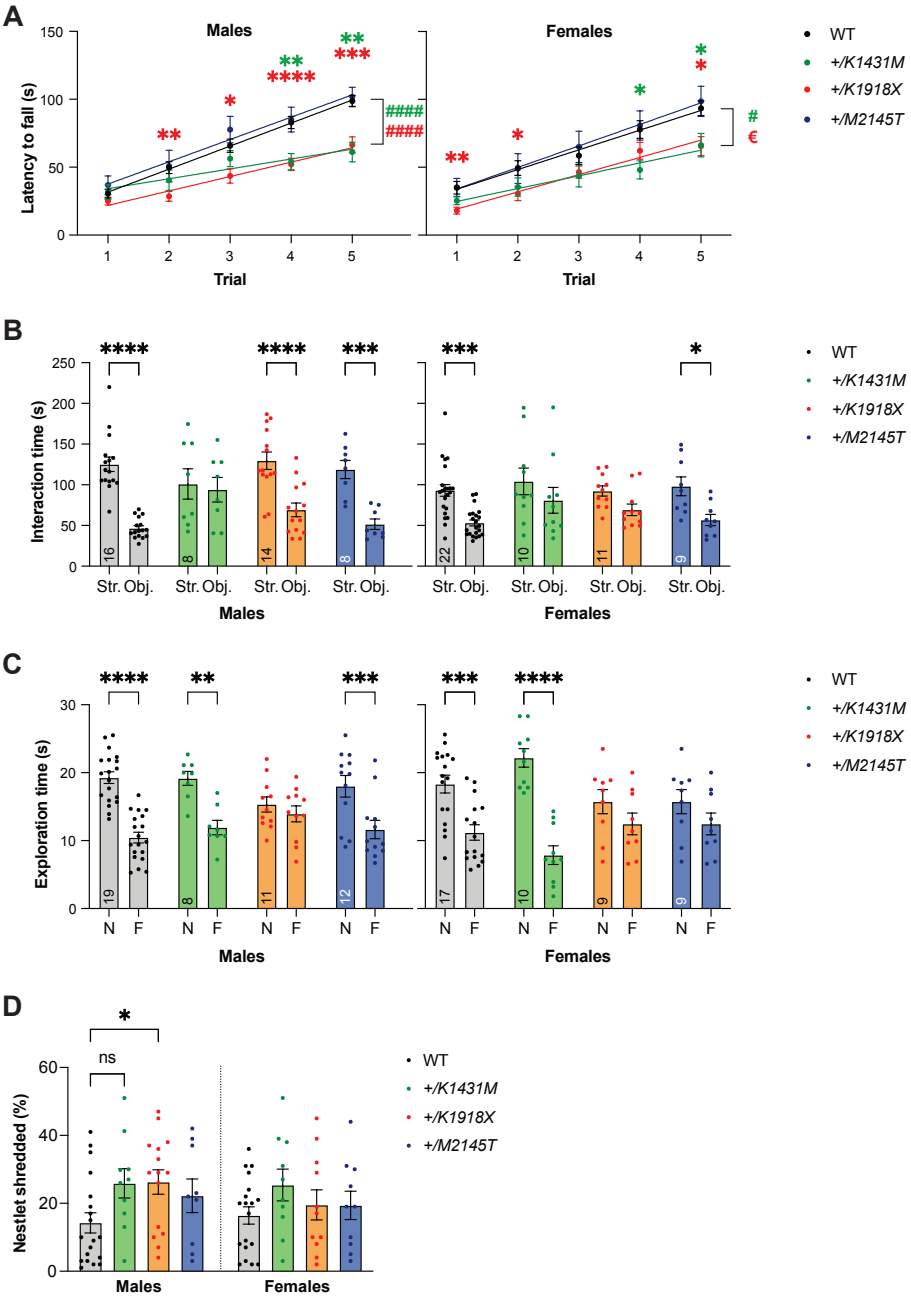

Fig. 2. Distinct *Trio* variants differentially impact NDD-like mouse behaviors.

(A) *+/K1431M* and *+/K1918X* mice of both sexes had decreased latency to fall off an accelerating rotarod compared to WT mice. Two-way ANOVA with post-hoc Bonferroni MC test identified differences from WT for each individual trial (*p<0.05, **p<0.01, ***p<0.001, ****p<0.0001). Linear regressions identified differences from WT in slopes (Males: *+/K1431M* 7.270 ±2.019, p<0.0001; *+/K1918X* 10.61 ±1.444, p<0.0001; vs WT 16.96 ±1.344; Females: *+/K1431M* 9.436 ±2.146, p=0.0215 vs WT 14.52 ±1.792; $^{\#}$p<0.05, $^{\#\#\#\#}$p<0.0001) and intercepts (Males: *+/K1431M* 26.93 ±6.696, p=0.0729; vs WT 14.65 ±4.458; Females: *+/K1918X* 6.492 ±5.555, p=0.0248; vs WT 19.28 ±5.942; $^{€}$p<0.05). n=40 male and 28 female WT; 10 male and 11 female *+/K1431M*; 16 male and 13 female *+/K1918X*; 13 male and 15 female *+/M2145T* mice. **(B)** WT mice displayed normal social preference and spent more time with a stranger mouse (Str.) relative to an inanimate object (Obj.) in a three-chamber interaction test. Social interactions were impaired in *+/K1431M* (both sexes) and *+/K1918X* (females only). **(C)** WT mice spent more time with a novel object (N) than with a familiar object (F). Novel object recognition was impaired in *+/K1918X* of both sexes and in *+/M2145T* females. **(D)** Male *+/K1918X* mice exhibited increased nestlet shredding over 30 minutes (26.63 ±3.61% shredded vs WT 14.26 ±2.97%; p=0.0332), and male *+/K1431M* mice exhibited a trend toward increased nestlet shredding (25.90 ±4.34% shredded, p=0.0861) compared to WT mice. n=19 male and 19 female WT; 10 male and 10 female *+/K1431M*; 15 male and 11 female *+/K1918X*; 9 male and 10 female *+/M2145T* mice. All data are presented as mean ±SEM. For **(B-D)**, two-way ANOVA with post-hoc Bonferroni MC test identified differences from WT (^{ns}p<0.1, *p<0.05, **p<0.01, ***p<0.001, ****p<0.0001). Numbers of mice quantified per group are annotated inside the bar.

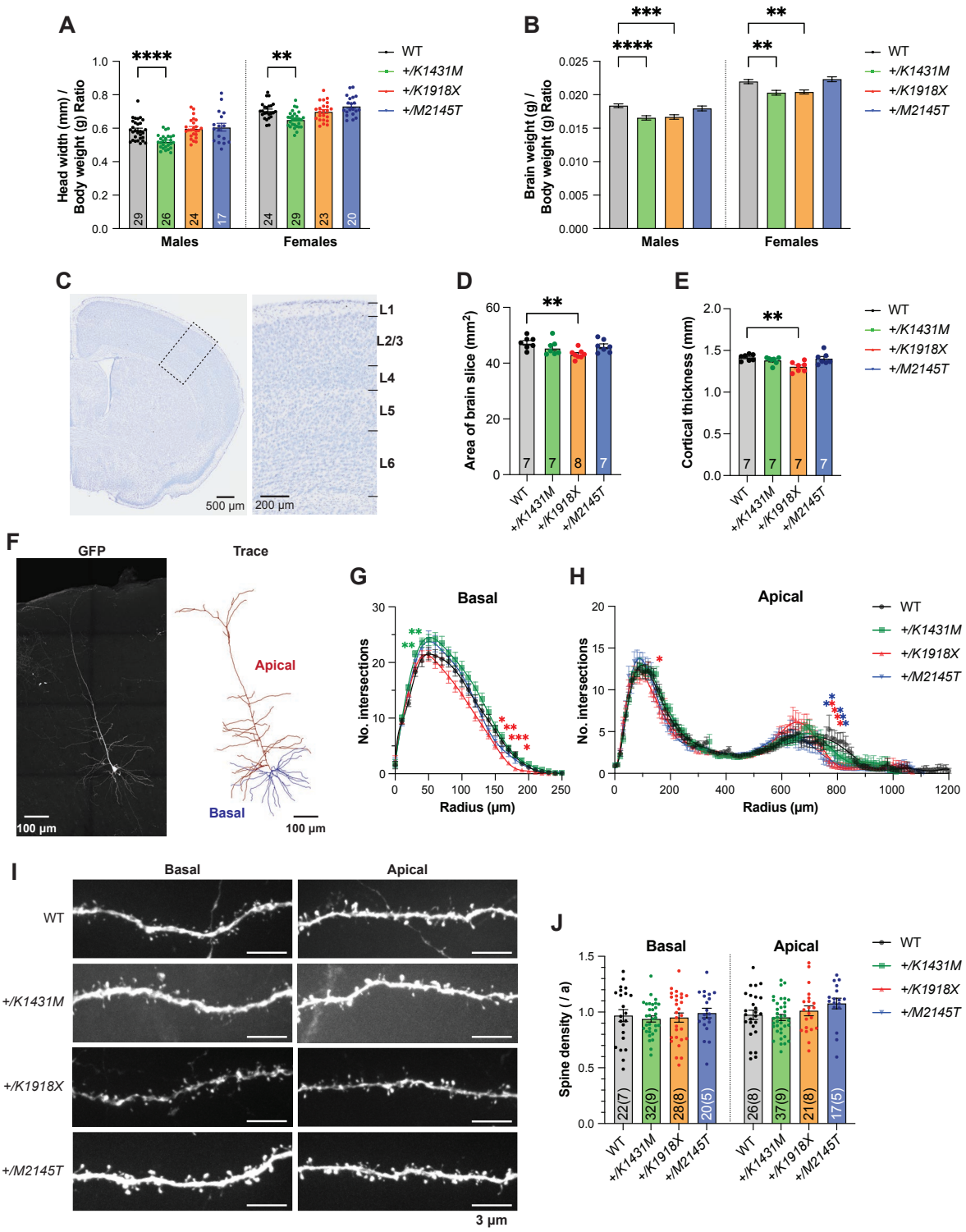

Fig. 3. *Trio +/K1431M* and *+/K1918X* mice have smaller brains, but only *+/K1918X* brains have smaller less complex neurons.

(A) Head widths of P42 *+/K1431M* mice were reduced (-11.8% males; -7.5% females) compared to WT mice after normalizing to body weight (males 0.520 ±0.008 mm/g vs WT 0.589 ±0.011 mm/g, p=0.0001; females 0.652 ±0.009 mm/g vs WT 0.705 ±0.010 mm/g, p=0.0144). Head width-to-body weight ratios were calculated per individual mouse, with

mouse number per group annotated within the bar. **(B)** Brain weights of P42 *+/K1431M* and *+/K1918X* mice were reduced (*+/K1431M* males -9.9%, females -7.6%; *+/K1918X* males -9.2%, females -7.1% compared to WT mice) after normalizing to body weight (males: *+/K1431M* 0.0165 ±0.0004, p=0.0002; *+/K1918X* 0.0167 ±0.0004, p=0.0015; vs WT 0.0184 ±0.0004; females: *+/K1431M* 0.0203 ±0.0004, p=0.0085; *+/K1918X* 0.0204 ±0.0003, p=0.0234; vs WT 0.0220 ±0.0004). Ratios were calculated by dividing the mean brain weight by the mean body weight of overlapping but non-identical populations of mice (see Supp. Fig.1 for mouse number per group). For (A,B), data are presented as mean ±SEM. Two-way ANOVA with post-hoc Bonferroni MC test identified differences from WT (*p<0.05, **p<0.01, ***p<0.001). **(C)** Representative Nissl-stained image of a 30 µm coronal slice from a P42 WT brain. Magnification of the cortex (dotted black box) reveals cortical layers. **(D)** Total cross-sectional brain area of Nissl-stained sections were reduced ~9% in P42 *+/K1918X* brains (43.21 ±0.577 mm^2 vs WT 47.29 ±0.823 mm^2, p=0.0045). **(E)** Total thickness of the cortex, in the region marked by the dotted black box in (C), is reduced ~8% in P42 *+/K1918X* brains (1.304 ±0.02262 mm vs WT 1.416 ±0.01417 mm, p=0.0021). For (D,E), data are presented as mean ±SEM. Ordinary one-way ANOVA with post-hoc Bonferroni MC test identified differences from WT (**p<0.01; n=number of mouse brains, annotated within the bar). **(F)** Representative maximum projection fluorescence image and corresponding dendritic arbor reconstruction of a motor cortex Layer 5 pyramidal neuron (M1 L5 PN) from a WT mouse. **(G-H)** Sholl analysis revealed basal (G) and apical (H) dendritic arborization changes in *Trio* variant M1 L5 PNs compared to WT: both basal and apical arborization was reduced in *+/K1918X*, while proximal basal arborization was increased in *+/K1431M*. Two-way ANOVA (stacked) with post-hoc Bonferroni MC test identified differences from WT at each radius centered at the soma (*p<0.05, **p<0.01, ***p<0.001; n=23 neurons from 17 WT mice, 22 neurons from 15 *+/K1431M* mice, 20 neurons from 12 *+/K1918X* mice, 20 neurons from 14 *+/M2145T* mice). **(I)** Representative maximum projection fluorescence images of basal and apical dendrite segments from M1 L5 PNs of P42 mice *Trio* variant mice. Scale bar = 3 µm. **(J)** Dendritic spine density on proximal apical and secondary basal dendrites are unchanged in *Trio* variant mice compared to WT. Data show mean ±SEM. Ordinary one-way ANOVA with post-hoc Bonferroni MC test identified differences from WT. 2-5 dendrites were sampled per neuron; 1-2 neurons were imaged per mouse. Numbers of dendrites quantified per group are annotated inside the bar (number of neurons in parentheses).

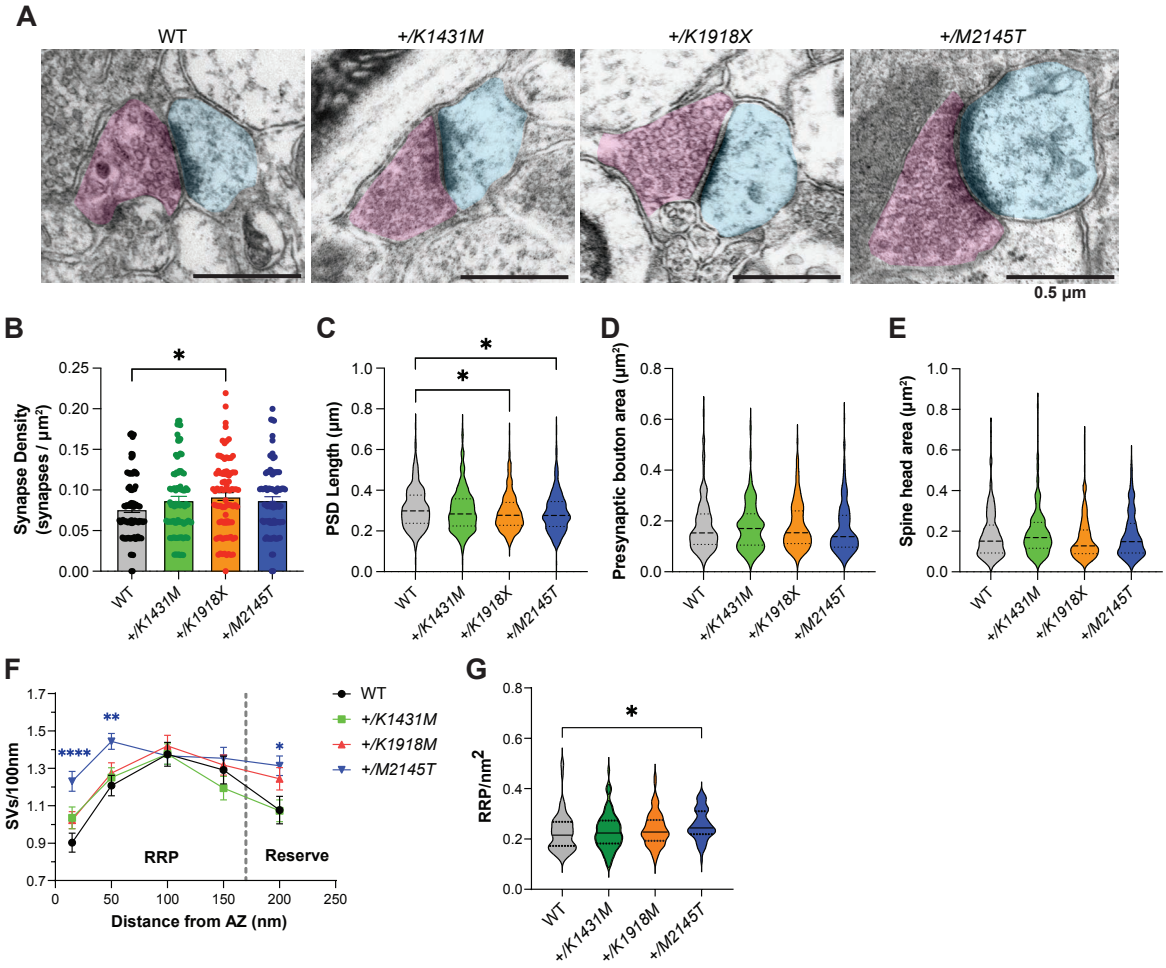

Fig. 4. *Trio* variants differentially impact synapse ultrastructure and synaptic vesicle distribution.

(A) Representative electron micrograph (EM) images from motor cortex layer 5 (M1 L5) of P42 WT and *Trio* variant mice. Post-synaptic regions are pseudo-colored in cyan; pre-synaptic regions in magenta. Scale bar = 0.5 µm. **(B)** Asymmetric synapses from all EM images of M1 L5 were quantified (from 18 fields of view per mouse, 5 mice per group). Synapse density was increased in *+/K1918X* mice (0.09205 ±0.004775 synapses/um^2; vs WT 0.07633 ±0.003954 synapses/um^2, p=0.0345). **(C)** PSD lengths were decreased in M1 L5 synapses of *+/K1918X* and *+/M2145T* mice (*+/K1918X* 0.2926 ±0.004652 um, p=0.0204; *+/M2145T* 0.2916 ±0.004922 um, p=0.0142; vs WT 0.3125 ±0.005612 um). **(D,E)** Presynaptic bouton and spine head areas of M1 L5 synapses were unchanged from WT in all *Trio* variants. **(F)** Synaptic vesicles (SVs) counted per 100 nm of active zone (AZ) length in M1 L5 as a function of distance from the AZ. *+/M2145T* showed an increase in docked (15 nm from AZ; 1.23 ±0.05 vs WT 0.90 ±0.05) and tethered SVs (50 nm from AZ; 1.44 ±0.04 vs WT 1.20 ± 0.05). *+/K1918X and +/M2145T* also showed an increase in the reserve pool of SVs (200 nm from AZ; 3.51 ±0.21 and 3.81 ±0.18, resp. vs WT 2.74 ±0.16). **(G)** Readily releasable pool (RRP),

calculated as number of SVs at 15-150 nm from AZ per area of distribution. RRP was significantly increased in *+/M2145T* (0.257 ±0.007 vs WT 0.228 ±0.008), driven by increased docked and tethered SVs. All data are presented as mean ±SEM. Ordinary one-way ANOVA with post-hoc Bonferroni MC test identified differences from WT (*p<0.05, **p<0.01, ***p<0.001, ****p<0.0001) For (C-F), n=number of synapses; for (G), 5 synapses per mouse were analyzed.

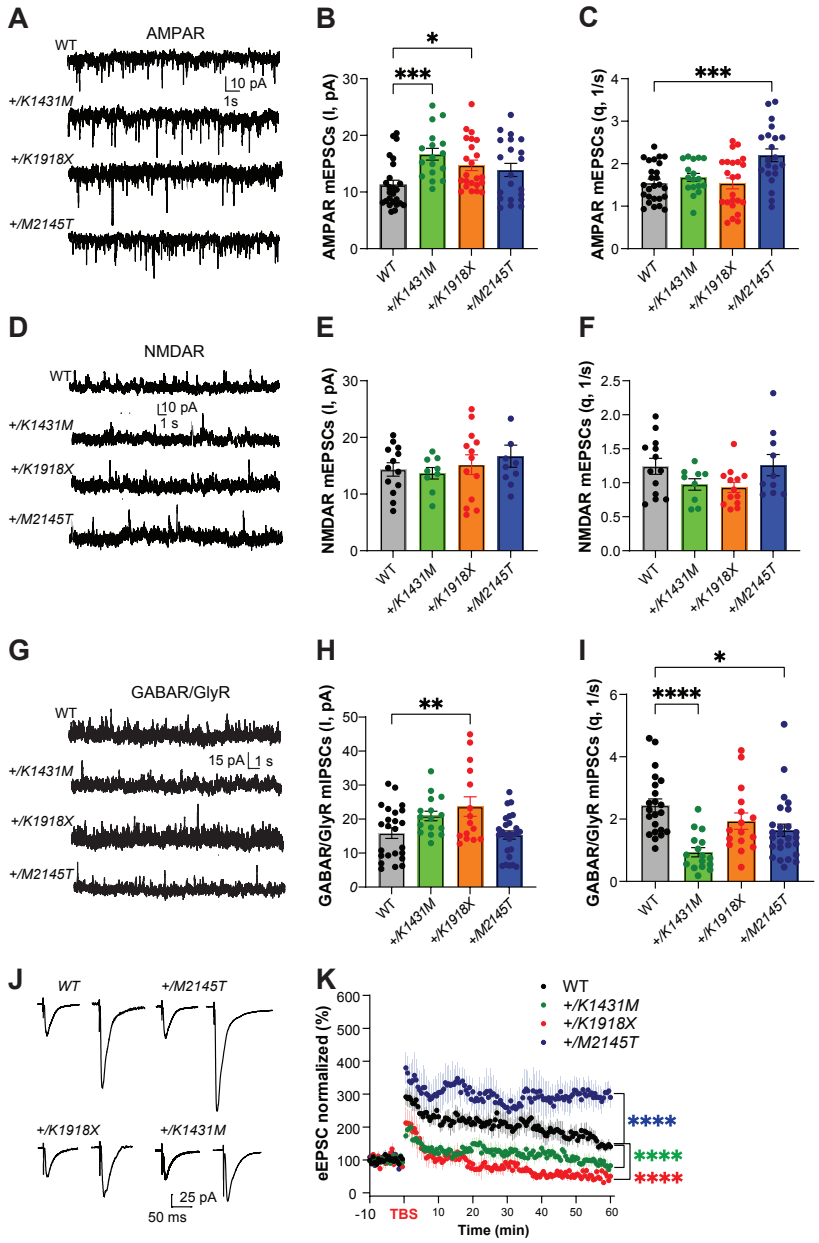

Fig. 5. *Trio* variant mice exhibit deficits in synaptic signaling and LTP.

(A, D, G) Representative traces of miniature excitatory and inhibitory postsynaptic currents (mEPSCs and mIPSCs) in M1 L5 pyramidal neurons of WT, *+/K1431M*, *+/K1918X* and *+/M2145T* mice. **(B)** AMPAR-mediated mEPSC amplitudes (I) were significantly increased in

+/K1431M (16.67 ±1.04 pA) and *+/K1918X* (14.71 ±0.92 pA) slices, with no observed changes in *+/M2145T* slices (13.90 ±1.16 pA) compared to WT (11.25 ±0.84 pA) (n=17-25 neurons from ≥6-8 mice per group). **(C)** No significant changes in AMPAR mEPSCs frequencies (q) were observed in *+/K1431M* and *+/K1918X,* while *+/M2145T* had an increase (2.20 ±0.15; vs WT 1.55 ±0.09). **(E, F)** No changes were observed in NMDAR mEPSCs amplitudes or frequencies (n=9-13 neurons from ≥5-7 mice per group). **(H, I)** GABA/GlyR mIPSCs amplitudes were significantly increased in *+/K1918X* vs WT (23.69 ±2.89 pA; vs 15.86 ±1.56 pA, resp.), while frequency was decreased in *+/K1431M* and *+/M2145T* (0.94 ±0.14 1/s and 1.64 ±0.19 1/s resp.; vs WT 2.44 ±0.20). (n=16-26 neurons from ≥6-8 mice per group). **(J)** Averaged representative traces of baseline and post-TBS eEPSCs currents in M1 L5 PNs of WT and *Trio* variant mice. Data are presented as mean ±SEM (*p<0.05; **p<0.01; ***p<0.001; ****p<0.0001). For **(B-J)**, one-way ANOVA with post-hoc Bonferroni test identified differences from WT. **(K)** Normalized eEPSCs amplitudes measuring LTP in L5 PNs by TBS in L2/3 afferents in all genotypes showed a significant decrease in the initiation and no potentiation of the LTP in *+/K1431M* and *+/K1918X*, with increase in initiation and potentiation of *+/M2145T* M1 L5 PNs compared to WT. LTP was induced at 0 min. RM two-way ANOVA with post-hoc Bonferroni MC test identified differences from WT (****p<0.0001; n=6-8 neurons from ≥4-5 mice per group).

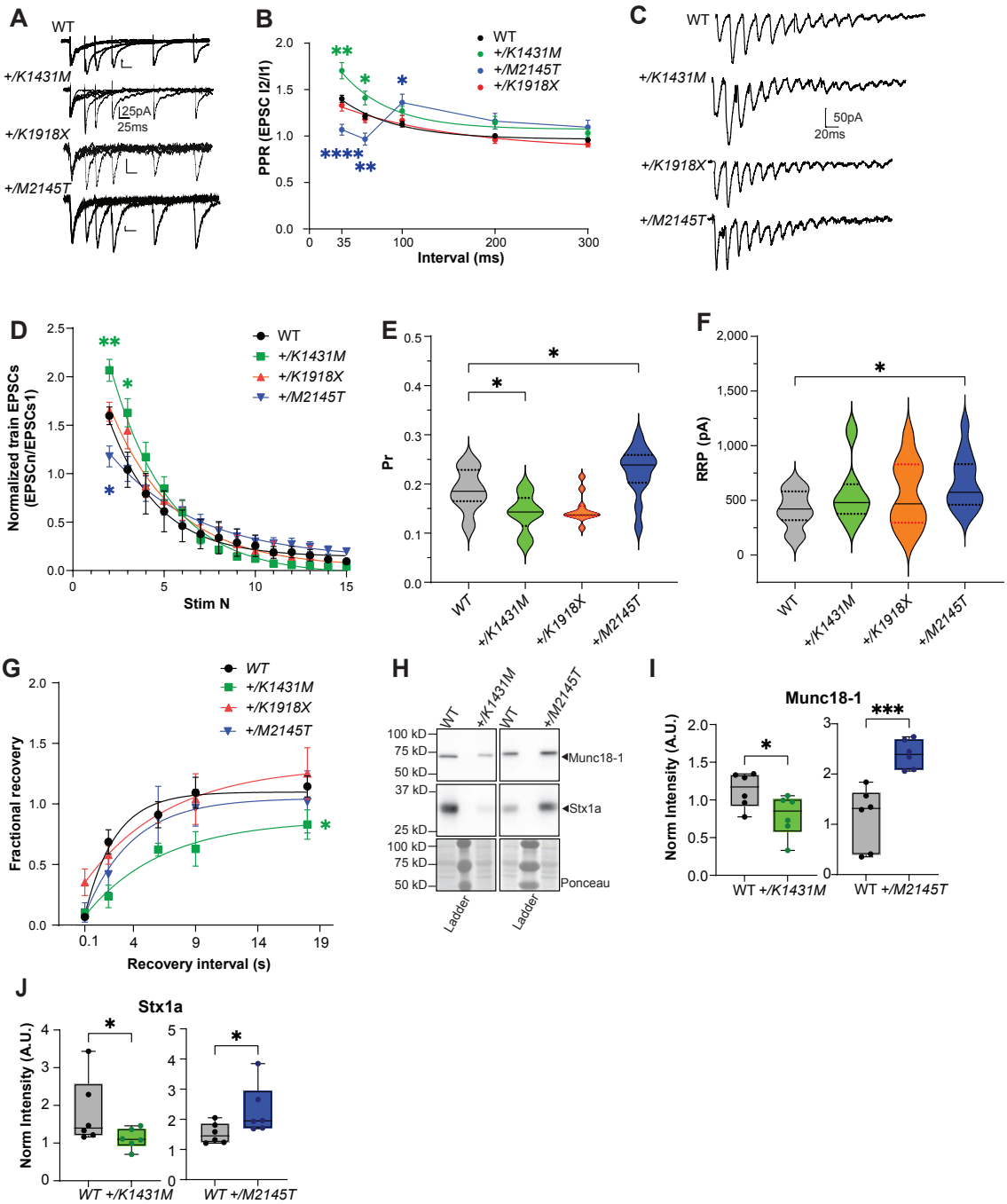

Fig. 6. *Trio* variant mice have deficiencies in short-term facilitation, glutamate Pr and RRP.

(A) Representative traces of paired stimulus in M1 L5 PNs of WT and *Trio* variant mice in response to paired pulse stimulation in the L2/3 M1. **(B)** Paired-pulse ratio (PPR) at varying interstimulus intervals (ISI), overlaid with a single exponential fit (except for *+/M2145T* data). An increase in the initial PPR was observed in M1 L5 PNs of *+/K1431M* mice (35 ms: 1.70 ±0.09, p=0.003; 60 ms: 1.42 ±0.07, p=0.046; n=20-34 neurons from ≥7-9 mice per group) with no change in *+/K1918X*; and in *+/M2145T* we observed a decrease in initial RRP at ISI (35 ms: 1.05 ±0.06, p<0.0001; 60 ms: 0.97 ±0.06, p=0.037) and an increase in later ISI (100 ms:

1.36 ±0.09, p=0.034; 200 ms: 1.18 ±0.08, p=0.013) compared to WT (35ms: 1.40 ±0.04; 60ms: 1.21 ±0.03; 100 ms: 1.13 ±0.03; 200 ms 1.0 ±0.02; 300 ms 0.96 ±0.17). **(C)** Representative traces of AMPAR eEPSCs in M1 L5 PNs under HFS (15 pulses at 40 Hz) in L2/3. **(D)** AMPAR $eEPSC_n$ amplitudes normalized to $eEPSC_1$ of the train revealed changes in the depletion rates during HFS in *Trio* variants compared to WT (tau decay (τ_d), WT: 2.7 s, *+/K1431M:* 3.2 s, *+/M2145T:* 4.8 s, *+/K1918X:* 3.5 s; n=11-13 neurons from 5 mice). **(E)** The estimated glutamate probability of release (Pr) was decreased in *+/K1431M* (0.14 ±0.01) and increased in *+/M2145T* (0.23 ±0.01), with no significant change in *+/K1918X* (0.15 ±0.01) compared to WT M1 L5 PNs (0.19 ±0.01; n=11-15 neurons from ≥ 5 mice per group). **(F)** The calculated size of the readily releasable vesicle pool (RRP) was increased in *+/M2145T* M1 L5 PNs compared to WT (665.7 ±68.5 pA and 415.8 ±43.9 pA, resp.; n=11-15 from ≥5 mice per genotype). **(G)** Exponential fits of the fractional recovery plotted vs ISI. Time of recovery, measured by exponential tau recovery (τ_R), showed significant decrease in *+/K1431M* M1 L5 PNs (5.5 s vs WT 2.2 s), graph also shows *+/K1431M* inability to fully recover to initial levels after ISI 18 s. **(H)** Representative immunoblots for Munc18-1 and Stx1a in P21 *+/K1431M* and *+/M2145T* cortical lysates. **(I,J)** Quantification of immunoblots demonstrated a reduction in both Munc18-1 and Stx1a protein in *+/K1431M* cortical lysates (-30% and -38%) and an increase in both proteins in *+/M2145T* (100% and 49%) compared to WT. Paired t-test identified differences from WT (*p<0.05, ***p<0.001; n=6 mice per genotype). Data are presented as mean ±SEM, with significant differences from WT tested using one-way ANOVA with post-hoc Bonferroni (D-G) or paired t-test (I,J) (*p<0.05; **p<0.01; ***p<0.001; ****p<0.0001).

REFERENCES

1. American Psychiatric Association. Diagnostic and Statistical Manual of Mental Disorders. 5th ed2013.

2. Brainstorm C, Anttila V, Bulik-Sullivan B, Finucane HK, Walters RK, Bras J, et al. Analysis of shared heritability in common disorders of the brain. Science. 2018;360(6395).

3. Wang T, Hoekzema K, Vecchio D, Wu H, Sulovari A, Coe BP, et al. Large-scale targeted sequencing identifies risk genes for neurodevelopmental disorders. Nat Commun. 2020;11(1):4932.

4. Carroll LS, Owen MJ. Genetic overlap between autism, schizophrenia and bipolar disorder. Genome Med. 2009;1(10):102.

5. Schlag F, Allegrini AG, Buitelaar J, Verhoef E, van Donkelaar M, Plomin R, et al. Polygenic risk for mental disorder reveals distinct association profiles across social behaviour in the general population. Mol Psychiatry. 2022;27(3):1588-98.

6. Doherty JL, Owen MJ. Genomic insights into the overlap between psychiatric disorders: implications for research and clinical practice. Genome Medicine. 2014;6.

7. Cross-Disorder Group of the Psychiatric Genomics C. Identification of risk loci with shared effects on five major psychiatric disorders: a genome-wide analysis. Lancet. 2013;381(9875):1371-9.

8. Ba W, Yan Y, Reijnders MR, Schuurs-Hoeijmakers JH, Feenstra I, Bongers EM, et al. TRIO loss of function is associated with mild intellectual disability and affects dendritic branching and synapse function. Hum Mol Genet. 2016;25(5):892-902.

9. Katrancha SM, Wu Y, Zhu M, Eipper BA, Koleske AJ, Mains RE. Neurodevelopmental disease-associated de novo mutations and rare sequence variants affect TRIO GDP/GTP exchange factor activity. Hum Mol Genet. 2017.

10. Ma XM, Huang JP, Eipper BA, Mains RE. Expression of Trio, a member of the Dbl family of Rho GEFs in the developing rat brain. J Comp Neurol. 2005;482(4):333-48.

11. McPherson CE, Eipper BA, Mains RE. Multiple novel isoforms of Trio are expressed in the developing rat brain. Gene. 2005;347(1):125-35.

12. Portales-Casamar E, Briancon-Marjollet A, Fromont S, Triboulet R, Debant A. Identification of novel neuronal isoforms of the Rho-GEF Trio. Biol Cell. 2006;98(3):183-93.

13. Ba W, van der Raadt J, Nadif Kasri N. Rho GTPase signaling at the synapse: implications for intellectual disability. Exp Cell Res. 2013;319(15):2368-74.

14. Bateman J, Van Vactor D. The Trio family of guanine-nucleotide-exchange factors: regulators of axon guidance. J Cell Sci. 2001;114(Pt 11):1973-80.

15. Bircher JE, Koleske AJ. Trio family proteins as regulators of cell migration and morphogenesis in development and disease - mechanisms and cellular contexts. J Cell Sci. 2021;134(3).

16. Grubisha MJ, DeGiosio RA, Wills ZP, Sweet RA. Trio and Kalirin as unique enactors of Rho/Rac spatiotemporal precision. Cell Signal. 2022;98:110416.

17. Kempers L, Driessen AJM, van Rijssel J, Nolte MA, van Buul JD. The RhoGEF Trio: A Protein with a Wide Range of Functions in the Vascular Endothelium. Int J Mol Sci. 2021;22(18).

18. Miller MB, Yan Y, Eipper BA, Mains RE. Neuronal Rho GEFs in synaptic physiology and behavior. Neuroscientist. 2013;19(3):255-73.

19. Paskus JD, Herring BE, Roche KW. Kalirin and Trio: RhoGEFs in Synaptic Transmission, Plasticity, and Complex Brain Disorders. Trends Neurosci. 2020;43(7):505-18.

20. Schmidt S, Debant A. Function and regulation of the Rho guanine nucleotide exchange factor Trio. Small GTPases. 2014;5:e29769.

21. Van Rijssel J, Timmerman I, Van Alphen FP, Hoogenboezem M, Korchynskyi O, Geerts D, et al. The Rho-GEF Trio regulates a novel pro-inflammatory pathway through the transcription factor Ets2. Biol Open. 2013;2(6):569-79.

22. O'Brien SP, Seipel K, Medley QG, Bronson R, Segal R, Streuli M. Skeletal muscle deformity and neuronal disorder in Trio exchange factor-deficient mouse embryos. Proc Natl Acad Sci U S A. 2000;97(22):12074-8.

23. Peng YJ, He WQ, Tang J, Tao T, Chen C, Gao YQ, et al. Trio is a key guanine nucleotide exchange factor coordinating regulation of the migration and morphogenesis of granule cells in the developing cerebellum. J Biol Chem. 2010;285(32):24834-44.

24. Zong W, Liu S, Wang X, Zhang J, Zhang T, Liu Z, et al. Trio gene is required for mouse learning ability. Brain Res. 2015;1608:82-90.

25. Katrancha SM, Shaw JE, Zhao AY, Myers SA, Cocco AR, Jeng AT, et al. Trio Haploinsufficiency Causes Neurodevelopmental Disease-Associated Deficits. Cell Rep. 2019;26(10):2805-17 e9.

26. Sun X, Wang L, Wei C, Sun M, Li Q, Meng H, et al. Dysfunction of Trio GEF1 involves in excitatory/inhibitory imbalance and autism-like behaviors through regulation of interneuron migration. Mol Psychiatry. 2021.

27. Tian C, Paskus JD, Fingleton E, Roche KW, Herring BE. Autism Spectrum Disorder/Intellectual Disability-associated mutations in Trio disrupt Neuroligin 1-mediated synaptogenesis. J Neurosci. 2021.

28. Paskus JD, Tian C, Fingleton E, Shen C, Chen X, Li Y, et al. Synaptic Kalirin-7 and Trio Interactomes Reveal a GEF Protein-Dependent Neuroligin-1 Mechanism of Action. Cell Rep. 2019;29(10):2944-52 e5.

29. Barbosa S, Greville-Heygate S, Bonnet M, Godwin A, Fagotto-Kaufmann C, Kajava AV, et al. Opposite Modulation of RAC1 by Mutations in TRIO Is Associated with Distinct, Domain-Specific Neurodevelopmental Disorders. Am J Hum Genet. 2020;106(3):338-55.

30. Bonnet M, Roche F, Fagotto-Kaufmann C, Gazdagh G, Truong I, Comunale F, et al. Pathogenic TRIO variants associated with neurodevelopmental disorders perturb the molecular regulation of TRIO and axon pathfinding in vivo. Mol Psychiatry. 2023;28(4):1527-44.

31. Gazdagh G, Hunt D, Gonzalez AMC, Rodriguez MP, Chaudhry A, Madruga M, et al. Extending the phenotypes associated with TRIO gene variants in a cohort of 25 patients and review of the literature. Am J Med Genet A. 2023;191(7):1722-40.

32. Pengelly RJ, Greville-Heygate S, Schmidt S, Seaby EG, Jabalameli MR, Mehta SG, et al. Mutations specific to the Rac-GEF domain of TRIO cause intellectual disability and microcephaly. J Med Genet. 2016;53(11):735-42.

33. Sadybekov A, Tian C, Arnesano C, Katritch V, Herring BE. An autism spectrum disorder-related de novo mutation hotspot discovered in the GEF1 domain of Trio. Nat Commun. 2017;8(1):601.

34. Singh T, Poterba T, Curtis D, Akil H, Al Eissa M, Barchas JD, et al. Rare coding variants in ten genes confer substantial risk for schizophrenia. Nature. 2022;604(7906):509-16.

35. Debant A, Serra-Pages C, Seipel K, O'Brien S, Tang M, Park SH, et al. The multidomain protein Trio binds the LAR transmembrane tyrosine phosphatase, contains a protein kinase domain, and has separate rac-specific and rho-specific guanine nucleotide exchange factor domains. Proc Natl Acad Sci U S A. 1996;93(11):5466-71.

36. Bellanger JM, Lazaro JB, Diriong S, Fernandez A, Lamb N, Debant A. The two guanine nucleotide exchange factor domains of Trio link the Rac1 and the RhoA pathways in vivo. Oncogene. 1998;16(2):147-52.

37. Blangy A, Vignal E, Schmidt S, Debant A, Gauthier-Rouviere C, Fort P. TrioGEF1 controls Rac- and Cdc42-dependent cell structures through the direct activation of rhoG. J Cell Sci. 2000;113 (Pt 4):729-39.

38. Duman JG, Mulherkar S, Tu YK, J XC, Tolias KF. Mechanisms for spatiotemporal regulation of Rho-GTPase signaling at synapses. Neurosci Lett. 2015;601:4-10.

39. Hall A. Rho GTPases and the actin cytoskeleton. Science. 1998;279(5350):509-14.

40. Luo L. Rho GTPases in neuronal morphogenesis. Nat Rev Neurosci. 2000;1(3):173-

80.

41. Nakayama AY, Harms MB, Luo L. Small GTPases Rac and Rho in the maintenance of dendritic spines and branches in hippocampal pyramidal neurons. J Neurosci. 2000;20(14):5329-38.

42. Newey SE, Velamoor V, Govek EE, Van Aelst L. Rho GTPases, dendritic structure, and mental retardation. J Neurobiol. 2005;64(1):58-74.

43. Terry-Lorenzo RT, Torres VI, Wagh D, Galaz J, Swanson SK, Florens L, et al. Trio, a Rho Family GEF, Interacts with the Presynaptic Active Zone Proteins Piccolo and Bassoon. PLoS One. 2016;11(12):e0167535.

44. O'Neil SD, Racz B, Brown WE, Gao Y, Soderblom EJ, Yasuda R, et al. Action potential-coupled Rho GTPase signaling drives presynaptic plasticity. Elife. 2021;10.

45. Howrigan DP, Rose SA, Samocha KE, Fromer M, Cerrato F, Chen WJ, et al. Exome sequencing in schizophrenia-affected parent-offspring trios reveals risk conferred by protein-coding de novo mutations. Nat Neurosci. 2020;23(2):185-93.

46. Kloth K, Graul-Neumann L, Hermann K, Johannsen J, Bierhals T, Kortum F. More evidence on TRIO missense mutations in the spectrin repeat domain causing severe developmental delay and recognizable facial dysmorphism with macrocephaly. Neurogenetics. 2021;22(3):221-4.

47. Bircher JE, Corcoran EE, Lam TT, Trnka MJ, Koleske AJ. Autoinhibition of the GEF activity of cytoskeletal regulatory protein Trio is disrupted in neurodevelopmental disorder-related genetic variants. J Biol Chem. 2022;298(9):102361.

48. Frankfurt M, Luine V. The evolving role of dendritic spines and memory: Interaction(s) with estradiol. Horm Behav. 2015;74:28-36.

49. Yang H, Wang H, Jaenisch R. Generating genetically modified mice using CRISPR/Cas-mediated genome engineering. Nat Protoc. 2014;9(8):1956-68.

50. Chen S, Lee B, Lee AY, Modzelewski AJ, He L. Highly Efficient Mouse Genome Editing by CRISPR Ribonucleoprotein Electroporation of Zygotes. J Biol Chem. 2016;291(28):14457-67.

51. Haeussler M, Schonig K, Eckert H, Eschstruth A, Mianne J, Renaud JB, et al. Evaluation of off-target and on-target scoring algorithms and integration into the guide RNA selection tool CRISPOR. Genome Biol. 2016;17(1):148.

52. Nagy A. Manipulating the mouse embryo : a laboratory manual. 3rd ed2003. x, 764 p. p.

53. Feng G, Mellor RH, Bernstein M, Keller-Peck C, Nguyen QT, Wallace M, et al. Imaging neuronal subsets in transgenic mice expressing multiple spectral variants of GFP.

Neuron. 2000;28(1):41-51.

54. Blaise AM, Corcoran EE, Wattenberg ES, Zhang YL, Cottrell JR, Koleske AJ. In vitro fluorescence assay to measure GDP/GTP exchange of guanine nucleotide exchange factors of Rho family GTPases. Biol Methods Protoc. 2022;7(1):bpab024.

55. Schiavo G, Stenbeck G, Rothman JE, Sollner TH. Binding of the synaptic vesicle v-SNARE, synaptotagmin, to the plasma membrane t-SNARE, SNAP-25, can explain docked vesicles at neurotoxin-treated synapses. Proc Natl Acad Sci U S A. 1997;94(3):997-1001.

56. Deacon RM. Measuring the strength of mice. J Vis Exp. 2013(76).

57. Omar MH, Kerrisk Campbell M, Xiao X, Zhong Q, Brunken WJ, Miner JH, et al. CNS Neurons Deposit Laminin alpha5 to Stabilize Synapses. Cell Rep. 2017;21(5):1281-92.

58. Rapanelli M, Frick LR, Xu M, Groman SM, Jindachomthong K, Tamamaki N, et al. Targeted Interneuron Depletion in the Dorsal Striatum Produces Autism-like Behavioral Abnormalities in Male but Not Female Mice. Biol Psychiatry. 2017;82(3):194-203.

59. Sfakianos MK, Eisman A, Gourley SL, Bradley WD, Scheetz AJ, Settleman J, et al. Inhibition of Rho via Arg and p190RhoGAP in the postnatal mouse hippocampus regulates dendritic spine maturation, synapse and dendrite stability, and behavior. J Neurosci. 2007;27(41):10982-92.

60. Paul CA, Beltz B, Berger-Sweeney J. The nissl stain: a stain for cell bodies in brain sections. CSH Protoc. 2008;2008:pdb prot4805.

61. Franklin KBJ, Paxinos G. Paxinos and Franklin's The mouse brain in stereotaxic coordinates. Fourth edition. ed2013. 1 volume (unpaged) p.

62. Levy AD, Xiao X, Shaw JE, Sudarsana Devi SP, Katrancha SM, Bennett AM, et al. Noonan Syndrome-Associated SHP2 Dephosphorylates GluN2B to Regulate NMDA Receptor Function. Cell Rep. 2018;24(6):1523-35.

63. Gonzalez-Forero D, Montero F, Garcia-Morales V, Dominguez G, Gomez-Perez L, Garcia-Verdugo JM, et al. Endogenous Rho-kinase signaling maintains synaptic strength by stabilizing the size of the readily releasable pool of synaptic vesicles. J Neurosci. 2012;32(1):68-84.

64. Ruiz R, Cano R, Casanas JJ, Gaffield MA, Betz WJ, Tabares L. Active zones and the readily releasable pool of synaptic vesicles at the neuromuscular junction of the mouse. J Neurosci. 2011;31(6):2000-8.

65. Thanawala MS, Regehr WG. Determining synaptic parameters using high-frequency activation. J Neurosci Methods. 2016;264:136-52.

66. Aleman A, Hijman R, de Haan EH, Kahn RS. Memory impairment in schizophrenia: a meta-analysis. Am J Psychiatry. 1999;156(9):1358-66.

67. Heinrichs RW, Zakzanis KK. Neurocognitive deficit in schizophrenia: a quantitative review of the evidence. Neuropsychology. 1998;12(3):426-45.

68. Ridley RM. The Psychology of Perseverative and Stereotyped Behavior. Progress in Neurobiology. 1994;44(2):221-31.

69. Kaufmann WE, Moser HW. Dendritic anomalies in disorders associated with mental retardation. Cereb Cortex. 2000;10(10):981-91.

70. Huttenlocher PR. Dendritic development in neocortex of children with mental defect and infantile spasms. Neurology. 1974;24(3):203-10.

71. Huttenlocher PR. Dendritic development and mental defect. Neurology. 1970;20(4):381.

72. Huttenlocher PR. Dendritic and synaptic pathology in mental retardation. Pediatr Neurol. 1991;7(2):79-85.

73. Purpura DP. Dendritic spine "dysgenesis" and mental retardation. Science. 1974;186(4169):1126-8.

74. Purpura DP. Dendritic differentiation in human cerebral cortex: normal and aberrant developmental patterns. Adv Neurol. 1975;12:91-134.

75. Kulkarni VA, Firestein BL. The dendritic tree and brain disorders. Mol Cell Neurosci. 2012;50(1):10-20.

76. Hutsler JJ, Zhang H. Increased dendritic spine densities on cortical projection neurons in autism spectrum disorders. Brain Res. 2010;1309:83-94.

77. Glantz LA, Lewis DA. Decreased dendritic spine density on prefrontal cortical pyramidal neurons in schizophrenia. Arch Gen Psychiatry. 2000;57(1):65-73.

78. Glausier JR, Lewis DA. Dendritic spine pathology in schizophrenia. Neuroscience. 2013;251:90-107.

79. Kolluri N, Sun Z, Sampson AR, Lewis DA. Lamina-specific reductions in dendritic spine density in the prefrontal cortex of subjects with schizophrenia. Am J Psychiatry. 2005;162(6):1200-2.

80. van Spronsen M, Hoogenraad CC. Synapse pathology in psychiatric and neurologic disease. Curr Neurol Neurosci Rep. 2010;10(3):207-14.

81. Blanpied TA, Ehlers MD. Microanatomy of dendritic spines: emerging principles of synaptic pathology in psychiatric and neurological disease. Biol Psychiatry. 2004;55(12):1121-7.

82. Penzes P, Cahill ME, Jones KA, VanLeeuwen JE, Woolfrey KM. Dendritic spine pathology in neuropsychiatric disorders. Nat Neurosci. 2011;14(3):285-93.

83. Purcell SM, Moran JL, Fromer M, Ruderfer D, Solovieff N, Roussos P, et al. A polygenic burden of rare disruptive mutations in schizophrenia. Nature. 2014;506(7487):185-90.

84. Satterstrom FK, Kosmicki JA, Wang JB, Breen MS, De Rubeis S, An JY, et al. Large-Scale Exome Sequencing Study Implicates Both Developmental and Functional Changes in the Neurobiology of Autism. Cell. 2020;180(3):568-+.

85. Genovese G, Fromer M, Stahl EA, Ruderfer DM, Chambert K, Landen M, et al. Increased burden of ultra-rare protein-altering variants among 4,877 individuals with schizophrenia. Nat Neurosci. 2016;19(11):1433-41.

86. Fromer M, Pocklington AJ, Kavanagh DH, Williams HJ, Dwyer S, Gormley P, et al. De novo mutations in schizophrenia implicate synaptic networks. Nature. 2014;506(7487):179-84.

87. De Rubeis S, He X, Goldberg AP, Poultney CS, Samocha K, Cicek AE, et al. Synaptic, transcriptional and chromatin genes disrupted in autism. Nature. 2014;515(7526):209-15.

88. Iossifov I, O'Roak BJ, Sanders SJ, Ronemus M, Krumm N, Levy D, et al. The contribution of de novo coding mutations to autism spectrum disorder. Nature. 2014;515(7526):216-21.

89. Pinto D, Delaby E, Merico D, Barbosa M, Merikangas A, Klei L, et al. Convergence of genes and cellular pathways dysregulated in autism spectrum disorders. Am J Hum Genet. 2014;94(5):677-94.

90. Kirov G, Pocklington AJ, Holmans P, Ivanov D, Ikeda M, Ruderfer D, et al. De novo CNV analysis implicates specific abnormalities of postsynaptic signalling complexes in the pathogenesis of schizophrenia. Mol Psychiatry. 2012;17(2):142-53.

91. Schultz-Rogers L, Muthusamy K, Pinto EVF, Klee EW, Lanpher B. Novel loss-of-function variants in TRIO are associated with neurodevelopmental disorder: case report. BMC Med Genet. 2020;21(1):219.

92. Howes OD, Cummings C, Chapman GE, Shatalina E. Neuroimaging in schizophrenia: an overview of findings and their implications for synaptic changes. Neuropsychopharmacology. 2023;48(1):151-67.

93. Dabiri M, Dehghani Firouzabadi F, Yang K, Barker PB, Lee RR, Yousem DM. Neuroimaging in schizophrenia: A review article. Front Neurosci. 2022;16:1042814.

94. Harvey I, Ron MA, Du Boulay G, Wicks D, Lewis SW, Murray RM. Reduction of cortical volume in schizophrenia on magnetic resonance imaging. Psychol Med.

1993;23(3):591-604.

95. Suddath RL, Casanova MF, Goldberg TE, Daniel DG, Kelsoe JR, Jr., Weinberger DR. Temporal lobe pathology in schizophrenia: a quantitative magnetic resonance imaging study. Am J Psychiatry. 1989;146(4):464-72.

96. Zipursky RB, Lim KO, Sullivan EV, Brown BW, Pfefferbaum A. Widespread cerebral gray matter volume deficits in schizophrenia. Arch Gen Psychiatry. 1992;49(3):195-205.

97. Kowluru A. Friendly, and not so friendly, roles of Rac1 in islet beta-cell function: lessons learnt from pharmacological and molecular biological approaches. Biochem Pharmacol. 2011;81(8):965-75.

98. Kowluru A. Multiple Guanine Nucleotide Exchange Factors Mediate Glucose-Induced Rac1 Activation and Insulin Secretion: Is It Precise Regulatory Control or a Case of Two Peas from the Same Pod? ACS Pharmacol Transl Sci. 2021;4(5):1702-4.

99. Zhou S, Yu D, Ning S, Zhang H, Jiang L, He L, et al. Augmented Rac1 Expression and Activity are Associated with Oxidative Stress and Decline of beta Cell Function in Obesity. Cell Physiol Biochem. 2015;35(6):2135-48.

100. Veluthakal R, Thurmond DC. Emerging Roles of Small GTPases in Islet beta-Cell Function. Cells. 2021;10(6).

101. Asahara S, Shibutani Y, Teruyama K, Inoue HY, Kawada Y, Etoh H, et al. Ras-related C3 botulinum toxin substrate 1 (RAC1) regulates glucose-stimulated insulin secretion via modulation of F-actin. Diabetologia. 2013;56(5):1088-97.

102. Sylow L, Nielsen IL, Kleinert M, Moller LL, Ploug T, Schjerling P, et al. Rac1 governs exercise-stimulated glucose uptake in skeletal muscle through regulation of GLUT4 translocation in mice. J Physiol. 2016;594(17):4997-5008.

103. Broadbelt K, Byne W, Jones LB. Evidence for a decrease in basilar dendrites of pyramidal cells in schizophrenic medial prefrontal cortex. Schizophr Res. 2002;58(1):75-81.

104. Black JE, Kodish IM, Grossman AW, Klintsova AY, Orlovskaya D, Vostrikov V, et al. Pathology of layer V pyramidal neurons in the prefrontal cortex of patients with schizophrenia. Am J Psychiatry. 2004;161(4):742-4.

105. Ramaswamy S, Markram H. Anatomy and physiology of the thick-tufted layer 5 pyramidal neuron. Front Cell Neurosci. 2015;9:233.

106. Ba W, Nadif Kasri N. RhoGTPases at the synapse: An embarrassment of choice. Small GTPases. 2017;8(2):106-13.

107. Pertz O. Spatio-temporal Rho GTPase signaling - where are we now? J Cell Sci. 2010;123(Pt 11):1841-50.

108. Tian C, Paskus JD, Fingleton E, Roche KW, Herring BE. Autism Spectrum Disorder/Intellectual Disability-Associated Mutations in Trio Disrupt Neuroligin 1-Mediated Synaptogenesis. The Journal of Neuroscience. 2021/09/09;41(37).

109. Wiens KM, Lin H, Liao D. Rac1 Induces the Clustering of AMPA Receptors during Spinogenesis. Journal of Neuroscience. 2005-11-16;25(46).

110. Cui D, Jiang X, Chen M, Sheng H, Shao D, Yang L, et al. Activation of Rac1 Has an Opposing Effect on Induction and Maintenance of Long-Term Potentiation in Hippocampus by Acting on Different Kinases. Frontiers in Molecular Neuroscience. 2021/08/31;14.

111. Herring BE, Nicoll RA. Long-Term Potentiation: From CaMKII to AMPA Receptor Trafficking. https://doiorg/101146/annurev-physiol-021014-071753. 2016-02-10;78(1).

112. Duman JG, Blanco FA, Cronkite CA, Ru Q, Erikson KC, Mulherkar S, et al. Rac-maninoff and Rho-vel: The symphony of Rho-GTPase signaling at excitatory synapses. Small GTPases. 2022;13(1).

113. Ferraro F, Ma X-M, Sobota JA, Eipper BA, Mains RE. Kalirin/Trio Rho Guanine Nucleotide Exchange Factors Regulate a Novel Step in Secretory Granule Maturation. Molecular Biology of the Cell. 2007/12;18(12).

114. Hong-Geller E, Cerione RA. Cdc42 and Rac Stimulate Exocytosis of Secretory Granules by Activating the Ip3/Calcium Pathway in Rbl-2h3 Mast Cells. The Journal of Cell Biology. 2000/02/02;148(3).

115. Lecuona E, Ridge K, Pesce L, Batlle D, Sznajder JI. The GTP-binding Protein RhoA Mediates Na,K-ATPase Exocytosis in Alveolar Epithelial Cells. Molecular Biology of the Cell. 2003/09;14(9).

116. Momboisse F, Lonchamp E, Calco V, Ceridono M, Vitale N, Bader M-F, et al. βPIX-activated Rac1 stimulates the activation of phospholipase D, which is associated with exocytosis in neuroendocrine cells. Journal of Cell Science. 2009/03/15;122(6).

117. Pathak R, Delorme-Walker VD, Howell MC, Anselmo AN, White MA, Bokoch GM, et al. The Microtubule-associated Rho Activating Factor GEF-H1 interacts with Exocyst complex to regulate Vesicle Traffic. Developmental cell. 2012/08/08;23(2).

118. Doussau Fdr, Gasman Sp, Humeau Y, Vitiello F, Popoff M, Boquet P, et al. A Rho-related GTPase Is Involved in Ca2+-dependent Neurotransmitter Exocytosis *. Journal of Biological Chemistry. 2000/03/17;275(11).

119. O'Neil SD, Rácz B, Brown WE, Gao Y, Soderblom EJ, Yasuda R, et al. Action potential-coupled Rho GTPase signaling drives presynaptic plasticity. eLife. 2021;10.

120. Keine C, Al-Yaari M, Radulovic T, Thomas CI, Ramos PV, Guerrero-Given D, et al. Presynaptic Rac1 controls synaptic strength through the regulation of synaptic vesicle priming. eLife. 2022;11.

121. Wang HG, Lu FM, Jin I, Udo H, Kandel ER, de Vente J, et al. Presynaptic and postsynaptic roles of NO, cGK, and RhoA in long-lasting potentiation and aggregation of synaptic proteins. Neuron. 2005;45(3):389-403.

122. He E, Wierda K, van Westen R, Broeke JH, Toonen RF, Cornelisse LN, et al. Munc13-1 and Munc18-1 together prevent NSF-dependent de-priming of synaptic vesicles. Nat Commun. 2017;8:15915.

123. Tang F, Xiao D, Chen L, Gao H, Li X. Role of Munc18-1 in the biological functions and pathogenesis of neurological disorders (Review). Mol Med Rep. 2021;23(3).

124. Vardar G, Salazar-Lazaro A, Zobel S, Trimbuch T, Rosenmund C. Syntaxin-1A modulates vesicle fusion in mammalian neurons via juxtamembrane domain dependent palmitoylation of its transmembrane domain. Elife. 2022;11.

125. Watanabe Y, Katayama N, Takeuchi K, Togano T, Itoh R, Sato M, et al. Point mutation in syntaxin-1A causes abnormal vesicle recycling, behaviors, and short term plasticity. J Biol Chem. 2013;288(48):34906-19.